UNIVERSITÀ DEGLI STUDI DI PADOVA

DIPARTIMENTO DI SCIENZE CHIMICHE

CORSO DI LAUREA MAGISTRALE IN CHIMICA

TESI DI LAUREA MAGISTRALE

Inkjet-printed SERS substrates to study reactions in a microfluidic setup

Relatore: Prof. Moreno Meneghetti

Correlatore: Dott. Lucio Litti

Controrelatore: Dott. Daniel Forrer

Laureanda: Francesca Toffanello
2022763

A.A. 2021-2022

Summary

Abstract

Studying the chemical reaction mechanisms and dynamics is one of the fundamental tasks in chemistry. Nevertheless, it becomes particularly challenging when the diffusion of the species and the reaction kinetic are on the same order of velocity. In this view, new approaches in which diffusion dynamics and reaction kinetics can be decoupled are of great interest. The objective of this thesis is therefore to develop a microfluidic setup for the purpose of studying flow reactions by the Surface-Enhanced Raman Scattering signals associated with the species involved. In contrast with studying reactions in batch, this method makes it possible to observe the evolution of the reaction in the spatial dimension, potentially showing the mixing of the reagents and the reaction as soon as it starts to occur. The base of the microfluidic chip was inkjet printed with a gold nanoparticles ink to obtain an efficient SERS substrate covering all the channel. The side walls of the chip were obtained by carved out brass, to make it reusable and less prone to molecular lateral diffusion/permeation (as it happens in PDMS). Finally, the base and the side walls were assembled with a silicone-based glue and closed with a thin glass cover slide. Micro-Raman measures were run during the reagents flow within the microfluidic device according to routines coded in Matlab environment. This setup was applied for a couple of binary mixtures, the first made of not-reacting dyes and the second made of two reacting species resulting in a Schiff base that was successfully detected by SERS along the microfluidic chip.

1 Introduction

1.1 Microfluidics

Microfluidics is defined as the science of fluids circulating in microsystems with dimensions up to hundreds of micrometres, and the engineering and manufacturing of devices to process and manipulate them[1].
It offers many benefits that stem both from the use of small volumes of fluid and from its different behaviour in such a small scale, enabling new degrees of control of chemical reactions and new possibilities for analytical purposes.

Initially, microfluidics originated from techniques developed for the semiconductor industry, extending the technology of microelectronics and MEMS (microelectromechanical systems) to chemical analysis[2]. The first applications of these technologies have in fact been in analytical chemistry, with the invention of the miniaturized systems used in gas-phase chromatography and high-pressure liquid chromatography during the 1970s. Two major driving forces have since fostered its development: molecular biology, with the need of high throughput, high sensitivity analytical methods for DNA sequencing and genomics, and on the other side the military need to create portable, field-deployable “lab on a chip” devices for chemical and biological weapons detection. The earliest microfluidic systems were made of silicon and glass, expensive and difficult to fabricate, but nowadays the emergence of new materials, such as PDMS (polydimethylsiloxane), and new techniques, such as soft lithography, has made it increasingly easier (and cheaper) to develop and manufacture prototypes directly in the lab, pushing the field forward [1].

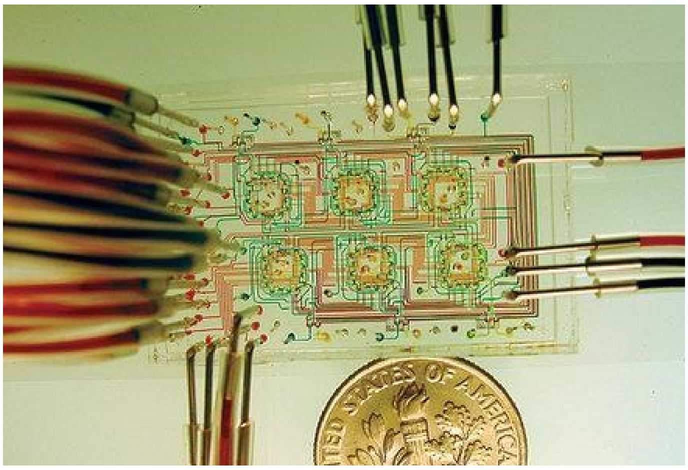

Figure 1.1.1: a microfluidic device used to study the growth of microbial populations.[1]

Microfluidic devices provide an environment in which fluids behave differently from the macroscale, due to the fact that fluid properties become progressively more controlled by viscous rather than inertial forces. The most important consequence of this is the absence of turbulence: the flow is essentially laminar, with Reynolds numbers typically <1000.

$$Re = \frac{\rho v D}{\gamma} \qquad [Eq. 1.1.1]$$

The Reynolds number (Re) is a dimensionless parameter that describes the ratio between inertial and viscous forces in a fluid. It is directly proportional to the characteristic velocity of the fluid v, the density ρ and the length scale of the system D, while inversely proportional to the fluid viscosity γ: this means that slower fluids travelling through narrower channels are more likely to be laminar. Re << 1 indicates that viscous effects dominate inertial effects, i.e. the flow is completely laminar, while Re >> 1 is characteristic of a turbulent flow, where inertial effects dominate viscous ones and fluids mix stochastically. In channel flows, Re < 1500-2000 indicates laminar flow [2].

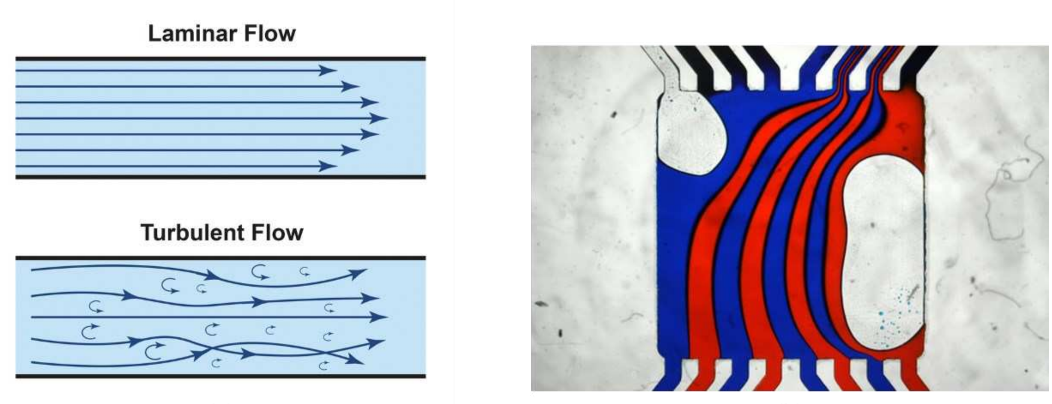

(a) (b)

Figure 1.1.2: (a) laminar versus turbulent flow[3]; (b) laminar flow around air bubbles (image taken from FolchLab picture gallery[4]).

Having laminar flow means that solvent particles move orderly in layers, which has consequences on how mixing occurs through the channel. On large scales fluids mix convectively, through turbulent movement caused by gradients of density, gravity or temperature, while on the microscale they flow in parallel and can only mix through diffusion across their interface. Diffusion between two different liquids is defined as the permeation of molecules from one side of the interface to the other, caused by their Brownian motion (random movements) driven by concentration gradients, for instance. Brownian motion of both solute and solvent molecules occurs everywhere in the liquid as the effect of thermal energy, even in the absence of the gradients cited above, but causes no apparent change in the bulk of each liquid due to the fact that all those molecules have the same properties[5]. A continuing diffusion however eventually causes the gradual distribution of the species through the interface. As this happens, the process progressively slows down, because the flux (J) of one species is proportional to its concentration gradient $\left(\frac{\partial C}{\partial x}\right)$, with the molecular diffusion coefficient (D) giving the proportional constant (first Fick's law).

$$J = -D\left(\frac{\partial C}{\partial x}\right) \qquad [Eq. 1.1.2]$$

The average distance travelled by a molecule through random movements (δ) is given by Equation 1.3, with D being the diffusion coefficient of the molecule:

$$\delta = \sqrt{2Dt} \qquad [Eq.\,1.1.3]$$

This equation shows why diffusion is so important in the microscale: a molecule such as haemoglobin (with D = 7 x 10^{-7} cm^{2}s^{-1}) in water will take 10^{6} seconds to diffuse 10 cm, but just 1 second to diffuse 10 μm.[6]

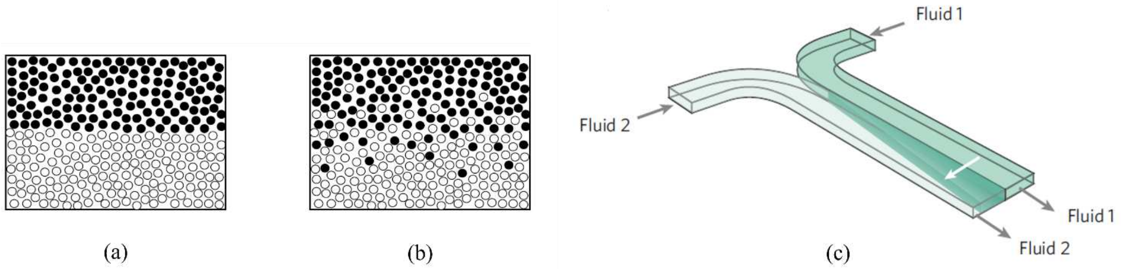

Figure 1.1.3: (a) interface between two fluids before diffusion; (b) interface during diffusion[5]*; (c) mixing of two miscible fluids under laminar flow conditions.*[7]

A laminar flow regime translates to highly predictable fluid dynamics and diffusion kinetics, while turbulent flow is unpredictable and disordered.

As already said, capillary forces and surface tension win against inertial forces (e.g. gravity) at the microscales: this is in fact what makes it possible for small insects to walk on water, and it gives interesting and useful characteristics to microfluidic systems.

Surface tension is the tendency of liquid surfaces to reduce their free energy by shrinking their surface area as much as possible, as a result of the cohesion between molecules on the liquid-gas interface. This phenomenon happens also between two immiscible fluids (but is called interfacial tension) and can be exploited to generate monodisperse bubbles or droplets in multiphasic systems (Figure 1.1.4).

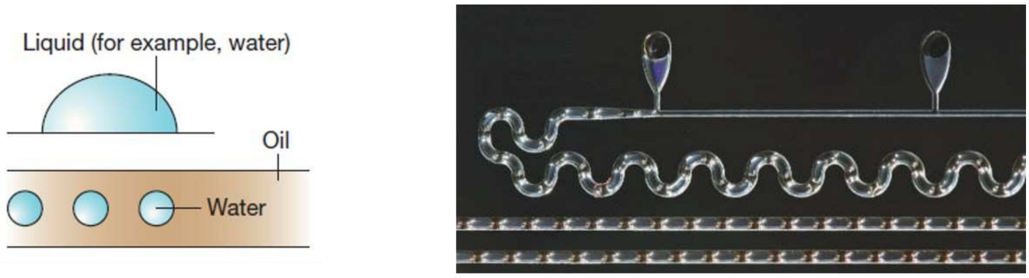

(a) (b)

Figure 1.1.4: (a) surface and interfacial tension[8]*; (b) channel sections of segmented gas-liquid flow in a microfluidic reactor for nanoparticle production.*[7]

These segmented flows find applications in protein and cell isolation and sorting, screening for protein crystallization conditions and even as microreactors for polymers and nanoparticle synthesis[1].

Fluidic microsystems in their simplest form consist of a component to introduce reagents in the chip and propel them, like syringe pumps and capillary tubes, a reactor unit where mixing and reaction occur, plus various other devices depending on the particular application (such as detectors for analysis, or purification elements for chemical synthesis).

Current methods of fabrication are primarily based on PDMS and soft lithography: microchannels are molded in the polymer from a master obtained by photolithography, 3D printing, micromachining and so on. The chip is then bonded to a flat surface, for example a glass slide. PDMS (polydimethylsiloxane) is a two-components polymer composed of an elastomer and a cross-linking agent. It is transparent, biocompatible, deformable and inexpensive, which made it the most commonly used polymer for microfluidic chips.

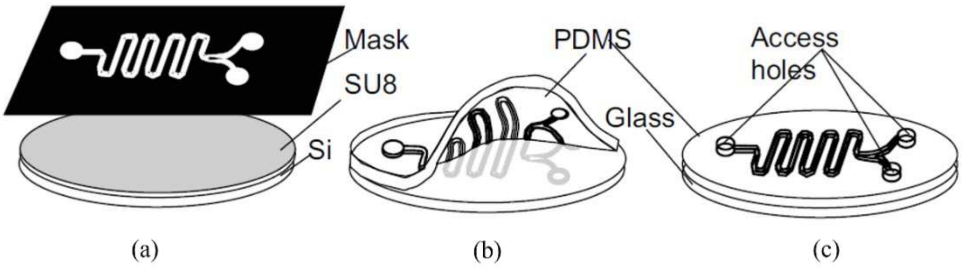

Figure 1.1.5: chip fabrication with soft lithography: (a) master developing by photolithography of silicon wafer; (b) poured PDMS is peeled off the master after hardening; (c) PDMS is bonded to the glass slide after treatment in oxygen plasma.[2]

Other manufacturing methods, often employed whenever PDMS does not fit with the specific application, include micromachining, injection molding, in situ fabrication and laser ablation. Micromachining of silicon and glass was one of the first techniques applied to microfluidics and allows for high precision chip fabrication but is expensive and requires highly specialized equipment.

1.1.1 Why microfluidics? Advantages and Applications

Microfluidic systems have the potential to impact on numerous fields of applications, from chemical synthesis and analysis to biology and medical diagnostics.

Microfluidics offers alternative routes of chemical synthesis, surpassing the intrinsic limitations of conventional batch systems, improving things like selectivity, reproducibility, safety and reagent consumption.[9] It allows for a greater control of reaction parameters like temperature and concentration gradients, since heat and mass transfer are faster and more efficient in such a limited scale. The high degree of temperature control reduces thermal decomposition of the desired product and, together with the high degree of mixing, prevents side reactions, improving yield, selectivity and purity.[10] Certain classes of reactions particularly benefit from flow conditions, for example:

- Runaway reactions, i.e. highly exothermic and autocatalytic reactions that require rapid cooling.

- Fast reactions for which the rate is diffusion-limited, so that efficient mixing is essential.
- Reactions which require high temperatures but happen in low-boiling solvents that can be superheated thanks to the relatively high pressure inside the microchannels.

Microreactors also minimize exposure risks for chemists that work with hazardous substances or dangerous reaction conditions, thanks to the very small quantities and minimal manipulation involved. Furthermore, processes can be automated and easily scaled-out, namely by using multiple reactors in parallel.[11]

In analytical chemistry the ultimate aim of microfluidics is to integrate several laboratory practices in a single chip, creating an individual device capable of separation, reaction and detection. These integrated chips are called lab-on-a-chip (LOCs) or µTAS (micro total analysis systems).

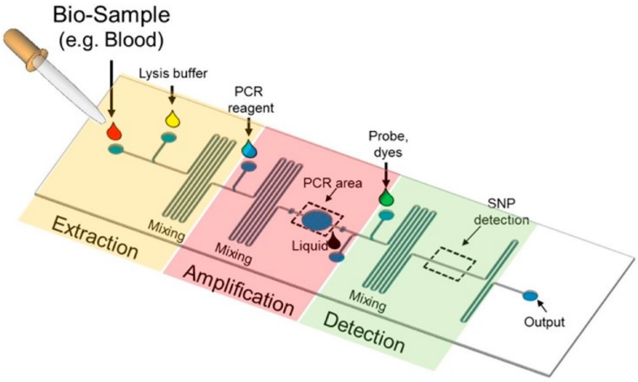

Figure 1.1.6: an example of LOC for genetic markers detection, with a zone for DNA extraction, one for amplification by PCR and finally one for detection.[12]

In respect to conventional analytical methods, miniaturized devices have the advantages of portability, small sample consumption, and allow for multiple measurement to be run in parallel.

Although many works have been published on this topic, the technology still hasn't reached widespread use. Major limiting factors are the difficulty in integrating sample preparation, which often requires a type of manipulation that is difficult to miniaturize, and detection, which usually requires off-chip machinery such as microscopes or mass spectrometers.[1]

The main application of microfluidic analytical systems has been in biochemical analysis and medical diagnostic. A well-known example, which does not involve channel manufacturing but takes advantage of capillarity, are lateral flow assays, like pregnancy tests or COVID-19 rapid antigen tests. Some of the benefits of microfluidic technology in these applications are cheapness, rapid processing of biofluids useful for research and clinical applications, and the possibility of creating *in vitro* models for drug discovery and diagnostics.[8]

1.1.2 Flow reactions analysis: process monitoring and reaction mechanisms study

Continuous processing in industrial settings requires precise reaction optimization to be convenient and cost-effective. Understanding the reaction mechanism, the potential side reactions, the rate of mixing and so forth is essential to choose the most efficient flow parameters and channel structure.

The conventional way to obtain kinetic and mechanistic data on flow reactions relies on offline measurements done with mass spectrometry, chromatography or NMR on collected samples. These methods however require manual intervention from a human operator and precise quenching and sampling of the reaction, thus risking artificial errors and compromised results.[13] A better accuracy is found with online and inline measurements, where the flow stream is automatically and regularly sampled, or where sensors or detection devices are placed directly within the channel (Figure 1.1.7). These methods can acquire real time data for process optimization, but inconsistency in physical parameters between where the reaction occurs and where the measurement takes place can adversely affect their precision and accuracy. A more accurate understanding of reaction mechanics can be found with *in situ* measurements, i.e. done directly in the reaction region.[14]

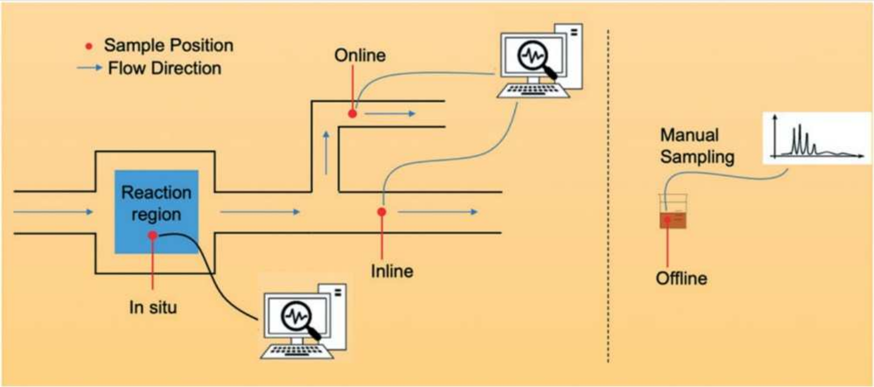

Figure 1.1.7: illustration of in situ, online, inline and offline measurements[14].

In situ analysis has the great advantage of allowing the monitoring of transient intermediates or unstable species that are formed during the progress of the reaction, providing meaningful evidence to determine the reaction mechanism. This is especially important with fast reactions (completed in less than 1s), reactions generating energetic intermediates and with those difficult to quench.

The most common method for *in situ* detection found in specialized literature is laser-induced fluorescence (LIF), appreciated for its sensitivity and simplicity. This technique however is limited to fluorescent molecules, so non fluorescent species need to be functionalized with a suitable chromophore. Moreover, it does not offer structural information like that obtainable, for example, with NMR or vibrational spectroscopy. [13]

Other analysis methods can be spectroscopy-based (FT-IR, NMR, UV-vis, Raman) or electrochemical, among others.

In general, studying the kinetics of a reaction in flow rather than in batch gives results more representative of the intrinsic kinetics of the systems, without being influenced by mass or heat transfer limitations. Moreover, it reduces experimental variance, facilitating the determination of rate models even for reactions with complicated mechanisms. One of its disadvantages however is the fact that a certain amount of residence time distribution must be accounted for, since laminar flow inside a microchannel creates a parabolic velocity profile (the closer the molecules are to channel walls, the slower they travel).[15]

Another advantage of flow devices is that each point along the channel corresponds to a different moment of the reaction: this means that a spatially resolved *in-situ* analysis (i.e. along the channel length) is able to obtain fundamental information tracing the entire progress of the reaction, in a single experiment.

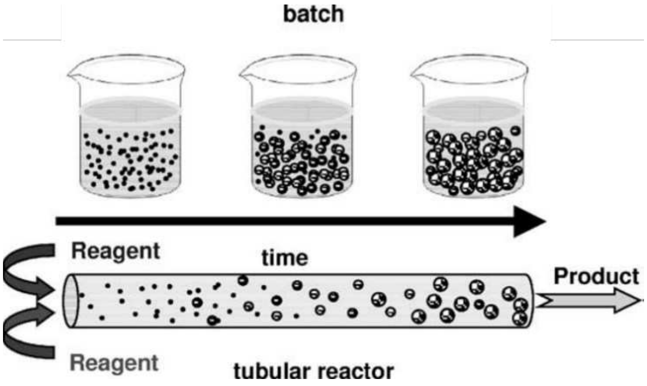

Figure 1.1.8: batch reactions versus flow reactions: conversion of time scale to spatial coordinate.[16]

Reaction imaging applied to microfluidic devices has been reported with optical methods such as bright-field microscopy, chemiluminescence imaging, spectroscopy-based microscopy, fluorescence-based microscopy, or even with temperature detection methods such as infrared thermography (for exothermic reactions).[17]

Both Infrared spectroscopy and Raman spectroscopy offer label-free and *in situ* imaging with high information content and high specificity.

FT-IR spectroscopy measures the absorption of infrared radiation by a sample, providing information on excited molecular vibrations that can be used to identify and characterize molecules based on their vibrational fingerprint. When coupled with microfluidics, this technique is used either in transmission mode, measuring transmitted radiation, or in attenuated total reflection (ATR) mode, where a high refractive index crystal is used to promote internal reflections of the incident IR beam and the detector records the attenuated beam reflected from the sample.[18]

Raman spectroscopy, which will be the subject of Chapter 1.2, also investigates molecular vibrations, but is based on the principle of inelastic scattering. It has a low sensitivity to water and is therefore particularly suitable for microfluidic applications running in aqueous environment. One of its drawbacks is that the Raman effect isn't very strong, in fact it's typically much weaker than fluorescence, producing signals with low intensity. A way to compensate for that is to use Surface Enhanced Raman Spectroscopy (SERS), a technique in which metallic nanoparticles are used to increase the sensitivity of Raman measures.

A relevant example of the combination of Raman spectroscopy and microfluidics is the work of Sarrazin et al.[19], who used confocal Raman spectroscopy to study the isotopic exchange reaction between H_2O and D_2O, creating spatially resolved concentration maps of the reagents and product (HOD) flowing in a Y shaped channel. Exploiting the high resolution of confocal microscopy, they were able to obtain three interconnected Raman images showing the molar fractions of H_2O, D_2O and HOD, observing the appearance of the product in the interdiffusion zone. Their method has the benefit of a very high spatial resolution in the micrometre range and worked very well with simple molecules, but may still be unsuitable for molecules with weak Raman signals, or with fluorescence emissions, due to the inherent limitations of Raman spectroscopy. Another instance of reaction imaging, this time employing SERS, can be found in the work of Xie et al.[20] In their study, they used the plasmonic and catalytic activity of bifunctional nanoparticles of Au-Pt-Au to investigate the reduction mechanism of $NaBH_4$, and in particular to underline its competition with the H_2 generated when it is used in protic solvents. Thanks to fast mixing and high temporal resolution offered by the microfluidic reactor, they were able to follow the fast (few seconds) reduction of 4-nitrothiophenol adsorbed on the colloidal nanoparticles, determining the rate constant of the reaction occurring at different pHs. However, using colloids as SERS substrates has a number of drawbacks, from the cruciality of having homogeneous mixing to obtain reproducible signals, to their instability and unwanted aggregation. In this respect the microfluidic platform developed in this thesis takes advantage of the signal enhancement of a 2D nanoparticles substrate, stable and consistent along the whole chip, to create Raman images spanning the entirety of the channel, showing the mixing of two reagents (pyridoxal 5'-phosphate and aniline-TACN) and the appearance of the product of their reaction (a Schiff base) thanks to their Raman signals.

1.2 Raman spectroscopy and SERS

1.2.1 Raman Spectroscopy

Raman spectroscopy is a vibrational spectroscopic technique that detects scattered radiation from molecules irradiated with monochromatic light, and correlates the difference in the energy of scattered photons with respect to the incident ones to the vibrational modes of the molecules.

The interaction of electromagnetic radiation with matter may lead to various phenomena:

- Absorption, if the energy of the incident photon corresponds to the energy gap between the ground state of the molecule and an excited state.
- Scattering, if the light brings the molecule into a virtual, unstable state by distorting the electron cloud around it, and is subsequently re-radiated in all directions. This is the phenomenon Raman spectroscopy is based on.

When only the electron cloud is distorted, the scattered radiation will have the same frequency of the incident one. This is called Rayleigh scattering (or elastic scattering) and is the predominant phenomenon when light meets molecules or particles much smaller than its wavelength. With a much lower occurrence, scattering can be inelastic: if the interaction induces nuclear motion so that there is a net transfer of energy between the radiation and the molecule, the scattered radiation will have a different energy from the incident one, corresponding to the gap between two vibrational states.[21] This phenomenon, called Raman scattering, was first discovered by Chandrasekhara Vankata Raman in 1921 and earned him the Nobel Prize in Physics.

The quantum theory of Raman scattering explains the phenomenon as the collision of a photon of the incident radiation with the molecule[22]. The incident photon induces a vibrational transition to a virtual excited state, created by the interaction between the molecule and the radiation. The system then can relax down to the ground state, or to an excited vibrational state. Scattering to an excited vibrational state emits a photon of lower energy than the incident one. There is an absorption of energy by the molecule and the diffused radiation has a lower frequency (Stokes scattering). Some molecules, however, may already be in an excited vibrational state due to thermal energy. In this case the molecules transfer energy to the scattered photon and the phenomenon is called anti-Stokes Raman scattering, but the generated signals are much lower because at room temperature most molecules are in the ground state.

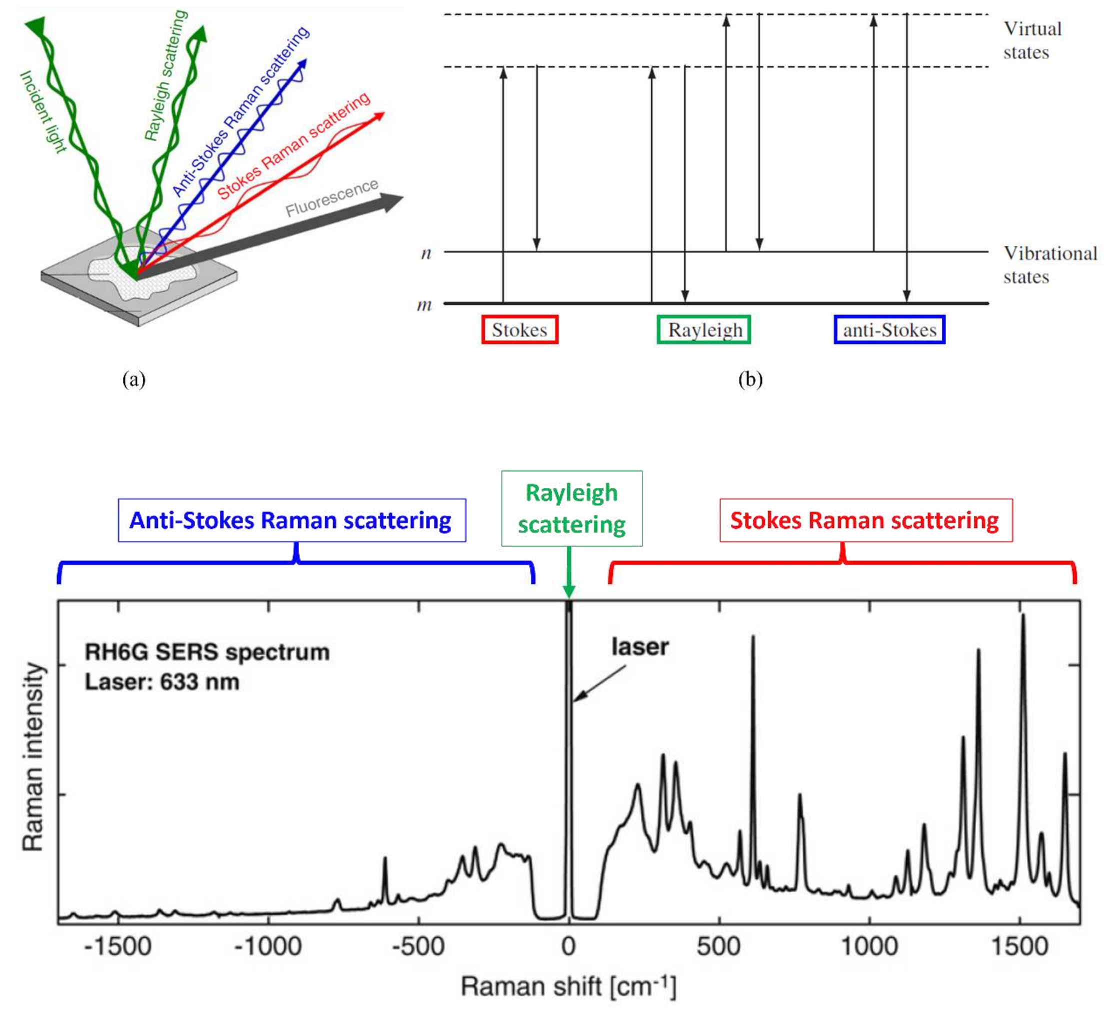

(a) (b)

(c)

Figure 1.2.1: (a) schematic representation of scattering phenomena after laser exposure[23]*; (b) vibrational energy diagram of the different types of scattering*[21]*; (c) a typical Raman spectrum, where Stokes and anti-Stokes signals are recognizable: their Raman shifts are symmetrical because they are ascribed to the same vibrational modes. At 0 cm*$^{-1}$ *is the signal of the Rayleigh scattering, which has the same energy of the incident laser. During usual Raman experiments only positive Raman shifts are visible, because an edge filter inside the spectrometer cuts the spectrum below 200 cm*$^{-1}$*.*[24] *Anti-Stokes scattering however can sometimes be preferred to avoid fluorescence interference (since fluorescence emission is always at a lower energy than the excitation frequency and therefore is on the right side of the spectrum).*

Raman spectra are measured by recording the intensity of the light inelastically scattered by a sample irradiated with a laser beam, resulting in a spectrum that shows the intensity of the Raman signal as a function of the Raman shift, i.e. the difference in wavenumber (cm^{-1}) between the incident light and the scattered light:

$$\Delta\bar{\nu}_{Raman} = \bar{\nu}_{ph} - \bar{\nu}_{scatter} \qquad [Eq. 1.2.1]$$

Peaks in the Raman spectrum correspond to vibrational modes of the molecule.

As said before, Raman scattering has a low probability to occur (only 1 photon every 10^6-10^8 undergoes inelastic scattering) and therefore is difficult to detect on its own. This has limited the applications of Raman spectroscopy for many years, slowing its development, but the discovery of lasers in 1969, and their application as high energy coherent sources, partially solved this problem and expanded the impact of the technique.

The classical theory of Raman scattering is going to be presented in the following.[22,25] The interaction between matter and electromagnetic radiation, specifically its electric field $\boldsymbol{E}$ (temporally resolved as in Equation 1.2.2, where ν_0 is the frequency, E_0 the maximum amplitude), perturbs the electronic cloud around the molecule and induces an electric dipole moment $\boldsymbol{\mu}^{ind}$, according to Equation 1.2.3, where α is the polarizability tensor, namely the tendency of the charge distribution to be distorted under a perturbation, like an electric field.

$$\boldsymbol{E} = E_0 cos(2\pi\nu_0 t) \qquad [Eq. 1.2.2]$$

$$\boldsymbol{\mu}^{ind} = \alpha\boldsymbol{E} \qquad [Eq. 1.2.3]$$

The molecular electronic distribution is governed by the relative positions of the atoms, thus a function of the molecular vibrations. It results that the polarizability can be expressed as a Taylor series expansion with respect to the normal coordinates of vibrations:

$$\alpha = \alpha_0 + \sum_i \left(\frac{\partial\alpha}{\partial Q_i}\right) Q_i + \frac{1}{2}\sum_{i,j}\left(\frac{\partial^2\alpha}{\partial Q_i \partial Q_j}\right) Q_i Q_j + \cdots \qquad [Eq. 1.2.4]$$

where α_0 is the polarizability at the equilibrium position and $Q_{i,j}$ are the normal coordinates of molecular vibration:

$$Q_i = Q_0 \, cos\,(2\pi\nu_i t) \qquad [Eq. 1.2.5]$$

Neglecting higher-order terms, and considering a single vibrational mode for simplicity, one obtains that the polarizability can be written as:

$$\alpha = \alpha_0 + \left(\frac{\partial \alpha}{\partial Q_i}\right) Q_i \qquad [Eq. 1.2.6]$$

Combining the different equations results in:

$$\boldsymbol{\mu}^{ind} = \left[\alpha_0 + \left(\frac{\partial \alpha}{\partial Q_i}\right) Q_0\, cos(2\pi \nu_i t)\ \right] E_0 cos(2\pi \nu_0 t) \qquad [Eq. 1.2.7]$$

Or, writing $\left(\frac{\partial \alpha}{\partial Q_i}\right) = \alpha_1$ and separating the three scattering terms:

$$\boldsymbol{\mu}^{ind} = \alpha_0 E_0 cos(2\pi \nu_0 t) +$$

$$+\frac{1}{2}\alpha_1 E_0 Q_0\, [\cos 2\pi\,(\nu_0 - \nu_i)t + \cos 2\pi\,(\nu_0 + \nu_i)t] \qquad [Eq. 1.2.8]$$

The first term is the Rayleigh scattering $\boldsymbol{\mu}^{ind}(\nu_0)$, where the induced dipole oscillates at the same frequency of the electric field that generates it, while the second and third represent the Raman scattering, respectively Stokes $\boldsymbol{\mu}^{ind}(\nu_0 - \nu_i)$, and anti-Stokes $\boldsymbol{\mu}^{ind}(\nu_0 + \nu_i)$.

From Equation 1.2.8 one may also highlight the Raman selection rules: to have a Raman active vibration, there must be a change in the polarizability of the electron cloud with respect to the vibrational coordinate, i.e. $\left(\frac{\partial \alpha}{\partial Q_i}\right) \neq 0$. This also means that the most intense Raman signals come from molecules with a lot of electrons, usually associated with higher polarizability, and especially from symmetric vibrations because they cause the greatest changes in the electron cloud. This is a very different situation compared to IR spectroscopy, where the selection rule requires a change in the permanent dipole moment, and usually asymmetric vibrations are the most intense. As a result of the different selection rules, Raman and IR spectroscopy may give rise to different vibrational peaks in their spectra, therefore offering complementary information. Centrosymmetric molecules, in particular, display the so-called mutual exclusion rule, namely not any vibration can be both IR and Raman active.

Other characteristics that distinguish Raman spectroscopy from IR spectroscopy are:

- Raman spectrometers may scan over a wider window, usually 3600-200 cm^{-1}, within a single measurement.
- Water and glass do not interfere on Raman measurements because O-H is a weak scatterer, allowing its use on samples in aqueous media.
- Most experiments use lasers in the visible range of the spectrum, which allows for a better spatial resolution in micro-spectroscopic experiments (since spatial resolution is directly proportional to the laser wavelength).

These characteristics make Raman spectroscopy seem more advantageous, but it isn’t without drawbacks:

- The low probability of the Raman scattering reflects on low Raman cross-sections, so that signals usually have low intensities. Raman measurements therefore require longer acquisition times (at the risk of burning the sample under the laser radiation) or even specific techniques like Resonant Raman (where resonance between the exciting radiation and electronic states makes the Raman effect more efficient) and other enhancement techniques (like SERS, discussed in detail in the following).
- Some molecules can fluoresce, masking the scattering signals.

Surface Enhanced Raman Spectroscopy, which will be presented in the next section, offers solutions to these problems.

1.2.2 SERS

Surface Enhanced Raman Spectroscopy (SERS) is a technique that can amplify Raman signals by several orders of magnitude due to the electromagnetic and chemical effects that occur when the molecule under investigation is absorbed on the surface of, mostly, plasmonic nanostructures, which can be either colloidal nanoparticles or nanostructured surfaces.

This effect was serendipitously discovered in 1974 by Fleischman *et al.*[26], when they observed a strong Raman scattering from pyridine molecules adsorbed on the surface of a roughened silver electrode.

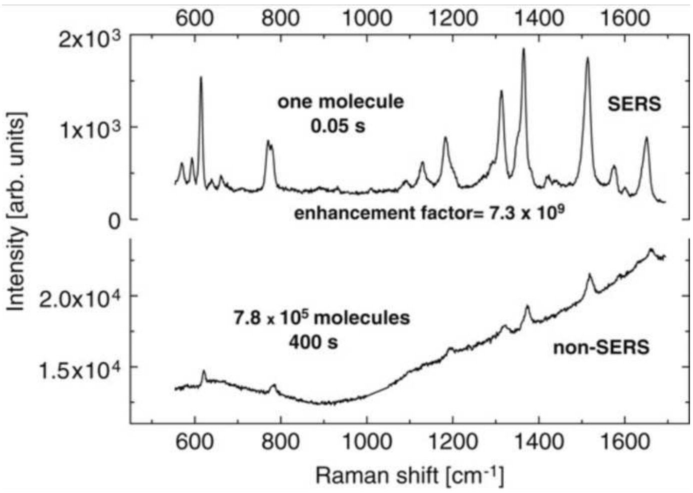

Figure 1.2.2: Raman and SERS spectra of Rhodamine 6G with 633 nm excitation.[22]

Over the years, many theories have been formulated to explain the surface enhancement phenomenon, but a unified one is still missing. It is currently believed that it is the result of two mechanisms, one chemical and one electromagnetic, that indeed play always together even if at different magnitude.

The electromagnetic theory explains the enhancement as the results of the resonant excitation of localized surface plasmons in the metal.

Metal structures contain conduction electrons held in place by the positively charged nuclei of the lattice. Strongly delocalized, they extend to a relatively considerable distance from the surface and have lateral freedom of movement along it. When electromagnetic radiation interacts with these free electrons, they collectively oscillate coherently with the field polarization. These collective oscillations of conduction electrons are called surface plasmons and can be described classically as a harmonic oscillator with its characteristic frequency ω_{SP}, which is related to the metal dielectric constant, but also to the surface geometry.[24]

On a flat surface, this oscillation propagates along the plane, but in nanoparticles (or nanostructured surfaces) with dimension smaller than the wavelength of the incident light, the surface plasmon is confined in a small region and the phenomenon is called localized surface plasmon.

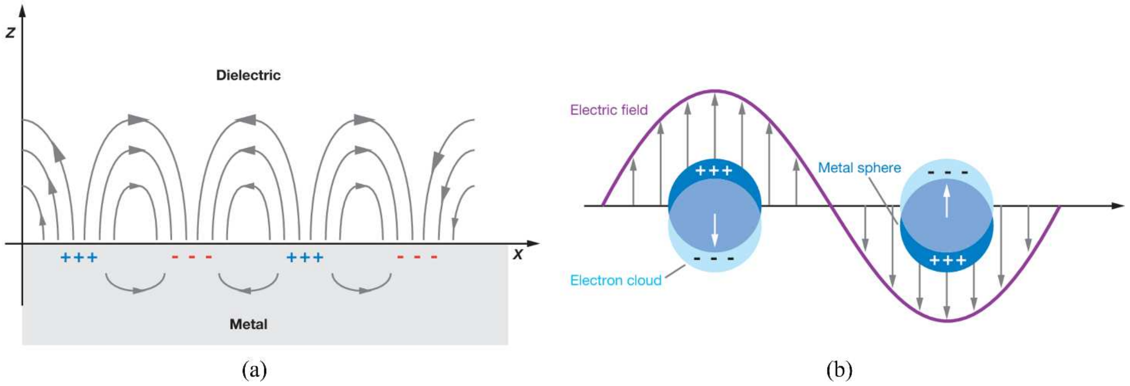

Figure 1.2.3: Schematic representations of (a) surface plasmons and (b) localized surface plasmons.[27]

When the incident laser excites the localized surface plasmons, the oscillating charges of the metal lattice form an additional electric field localized on the nanostructure surface. This can result in the amplification of both the exciting radiation and the scattering of neighbouring molecules.

The local electric field generated by a small metal nanoparticle on a nearby molecule is proportional to the incident field (E_0) and depends on the sphere radius (r) and on its distance (d) from the molecule:

$$E_{SP} = \frac{\varepsilon(\nu) - \varepsilon_0}{\varepsilon(\nu) + 2\varepsilon_0}\left(\frac{r}{r+d}\right)^3 E_0 \qquad [Eq. 1.2.4]$$

where ε_0 is the environment dielectric constant and $\varepsilon(\nu)$ is the metal dielectric constant. The molecule then feels an amplified incident field E_{LOC} given by $E_0 + E_{SP}$, maximised when it's adsorbed on the metal surface (i.e. minimal distance). The same enhancement happens also for the scattered Raman radiation. When both the laser and the scattered radiation are in resonance with the LSP (i.e.

when $\varepsilon(\nu) \approx -2\varepsilon_0$) the local electric field is at its maximum and the SERS enhancement is particularly strong: in this condition, called Localized Surface Plasmon Resonance (LSPR), the signal power increases with $|E_{LOC}|^4$ (this in an approximation in which the Raman shift is neglected and the incident and the scattered field amplitudes are averaged).[28]

SERS can be obtained with a single nanoparticle, but even bigger enhancement can be obtained when more elaborate structures are used. Anisotropic and spiky particles, junctions and small gaps between nanoparticles, all produce the so-called hotspots: small zones in which constructive interference of LSP enables enhancements as large as 10^{15} orders of magnitude[29].

At the single-particle level, anisotropic morphologies give the biggest enhancement factors, but when considering close-packed surfaces, simple morphologies (like spherical nanoparticles) significantly increase the SERS effect. In fact, the substrate fabricated during this thesis work was made by printing an ink of mostly spherical gold nanoparticles, but their close-packed deposition allowed for enhancement factors over 10^5, as demonstrated by previous studies of the guesting group.[30]

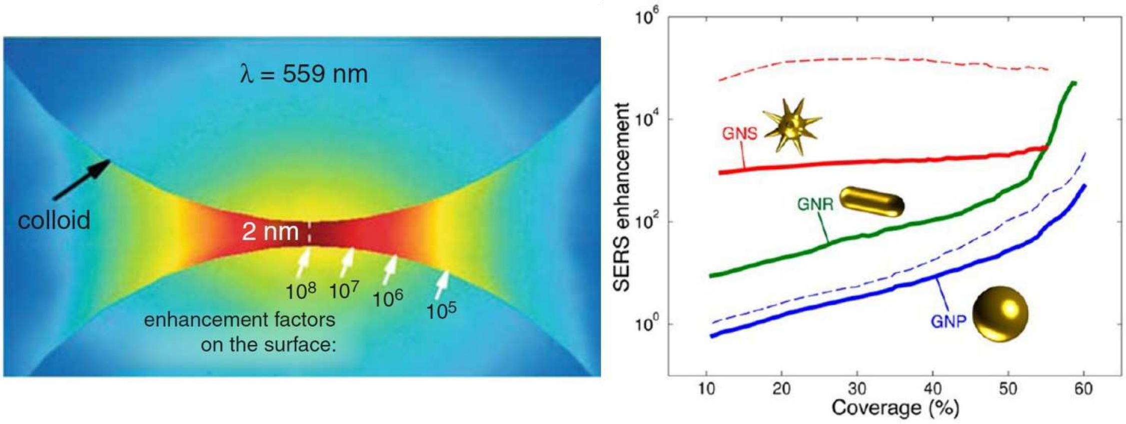

(a) (b)

Figure 1.2.4: (a) hotspot formed between two close nanoparticles. The SERS enhancement factor is strongly dependent on the distance between them[29]*; (b) predicted SERS enhancement factors for differently shaped nanoparticles, as a function of surface coverage.*[31]

The other mechanism theorized to explain SERS enhancement, the chemical enhancement, is mainly associated with charge transfers between the metal substrate and the absorbed molecule. The formation of this surface species significantly increases the molecule polarizability, thanks to the new electronic states formed through these interactions, since they provide new “channels” for the polarizability to be modified. Even without the formation of these surface complexes, the presence of the metal perturbs the electronic distribution of the molecule, which can result in a corresponding change in polarizability and thus scattering efficiency. Still, this chemical enhancement is thought to contribute little to the overall SERS effect, rarely more than a factor of 10. [24]

1.3 Inkjet printing of SERS substrates

SERS substrates can be colloidal suspensions of nanoparticles or planar metallic nanostructures. Today, the latter seem to be the preferred method due to their greater stability and reproducibility. Various techniques are used to produce them, such as thin-film deposition and nanolithography, but a cost-effective and user-friendly technique is inkjet printing of metal inks.

1.3.1 Gold nanoparticles: characteristics and production

Metal nanoparticles are essential to SERS, but not all of them work the same: the most suitable for this application are gold and silver nanoparticles. These two metals in fact have their plasmon resonance frequency in the visible and near-infrared range, while most other metals resonate in the ultraviolet region. In addition, gold is one of the least reactive chemical elements, making it the metal of choice for biological applications.

Colloidal gold has been used and researched for centuries. Its colour properties made it a fascinating object and prompted its use both in medicine and in art: red gold colloids were believed to have healing properties for having the same colour as blood and were therefore equated with vital essence.[32] Since roman times it has been used to colour glass, obtaining a range of colours from yellow to blue. Gold nanoparticles suspensions indeed have a different colour from the macroscopic material due to the already mentioned LSPR, and depending on their size and shape they can go from a deep red to violet/blue.

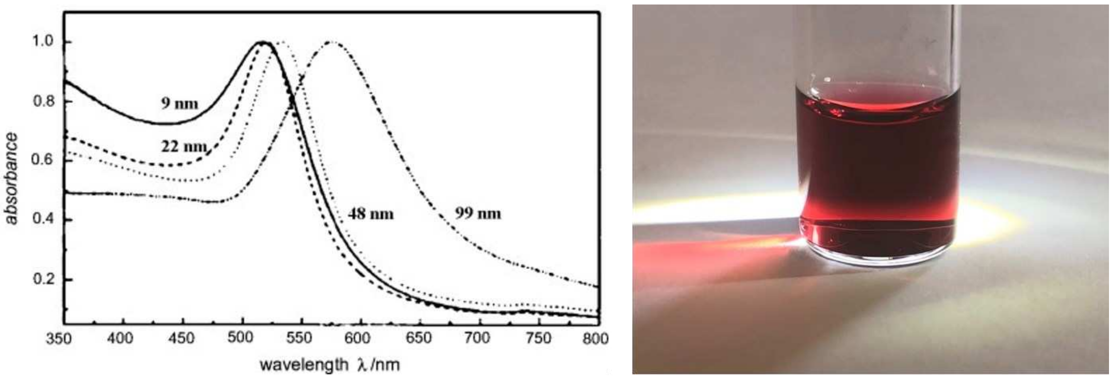

(a)

(b)

Figure 1.3.1: (a) absorption spectrum of gold nanoparticles of different sizes[33]*. When their diameter is approximately 20 nm, the SPR wavelength is around 522 nm, in the green region of the visible spectrum. The colloidal solution (b) therefore appears red in colour. An increase in size broadens the peak and moves it towards higher wavelengths (red shift).*

Production of metal colloids can be done either starting from the bulk material (top-down methods) or from molecular precursor by wet chemistry processes (bottom-up methods). After creating the nanoparticles, both methods require a mechanism to stabilize them, because electrostatic and van der Waals forces will push them together until they eventually precipitate out of solution. These mechanisms are mainly steric stabilization, where polymers or surfactants (called capping agents) are absorbed on the surface of the nanoparticles, or electrostatic stabilization, where particles repel each other thanks to surface charges.[34]

Bottom-up methods are based on the reduction and nucleation of dissolved metal cations into larger particles. One example of a bottom-up method is the reduction of chloroauric acid ($HAuCl_4$) by sodium citrate, which acts both as a reductive agent and as stabilizer to stop their growth and to prevent their aggregation.

Top-down methods, on the other hand, are mainly of three types: mechanical milling, sputtering and laser ablation. The latter is the technique used to produce the nanoparticles for this work, thus it will be briefly described in the next paragraph.

Laser ablation produces nanoparticles from a metal target (immersed in a solvent) by blasting it with a pulsed laser beam, usually with a duration in the order of nanoseconds or below. With a ns-pulse, a small region of the metal surface absorbs the laser beam energy, heats up and ejects matter in the form of plasma, confined near the surface thanks to the solvent. Expansion and subsequent cooling of the plasma below the boiling point of the metal leads to condensation of the ablated species, which form nucleation sites for the growth of nanoparticles.[35] The majority of the final nanoparticles have a spherical shape, with average sizes of 3–30 nm, but areas of fast cooling of the plasma may lead to asymmetric shapes.[36] The nanoparticles produced in this fashion are stable, as their surface presents an excess of negative charges due to partial oxidation of surface atoms that prevents their aggregation. Nanoparticle production by laser ablation is therefore a "green" method that doesn't require precursor or capping agents, leading to easily functionalisable particles.

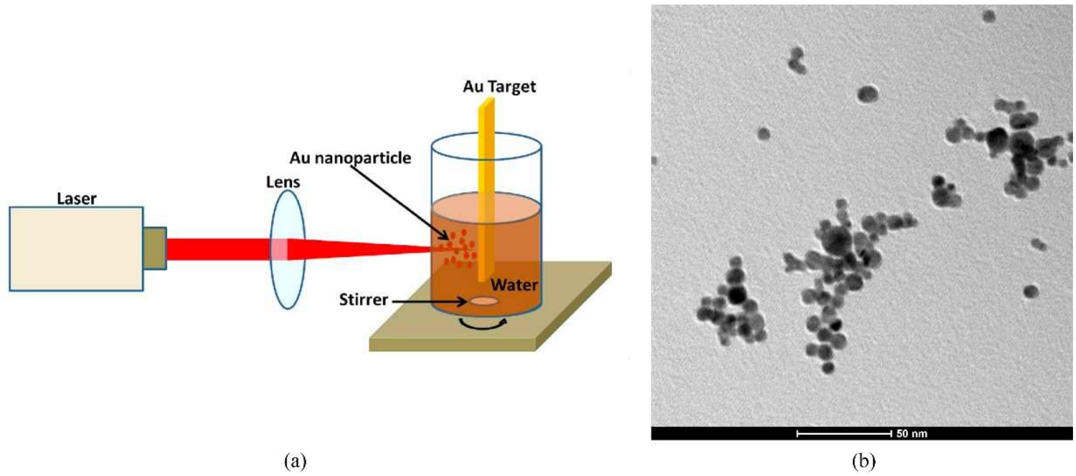

Figure 1.3.2: (a) schematic representation of laser ablation apparatus[37]; (b) TEM image of particles produced by laser ablation.

1.3.2 Inkjet printing

Printing is defined as the reproduction of a pattern on a substrate by controlled deposition of a material. Among the various types of printing, inkjet printing is particularly interesting because it deposits liquid inks, droplet-by-droplet directly on the substrate, without the need of a mask, which makes it flexible both in terms of substrates and pattern switching. Moreover, it doesn't require a lot of ink (especially compared to screen printing), it's easy to scale-up and has a high degree of reproducibility. Since its development in the 1970s, inkjet printing technology has achieved worldwide popularity and has recently evolved beyond graphics and paper, finding application in a variety of fields, from electronics to tissue engineering.[38, 39].

Two main families of inkjet printers are in use: continuous inkjet, which produces a constant stream of droplets and is mainly used in the packaging industry, and drop-on-demand (DOD) inkjet, which only produces droplets when required and it's the most common printer type in home and laboratory settings. DOD inkjets are of two kinds, depending on the mechanism of droplet generation. Thermal inkjets employ a resistor in the ink chamber to cause the formation of bubbles which move the ink out of the printhead. Piezoelectric inkjets, on the other hand, have a piezoelectric actuator that causes a pressure pulse in the ink chambre, stimulating the ejection of a drop. The voltage applied to the piezo controls the volume and velocity of the droplets, while the shape of the pulse (namely the time for which the potential is applied and its ascending and lowering gradients) can be adjusted by modifying its waveform.

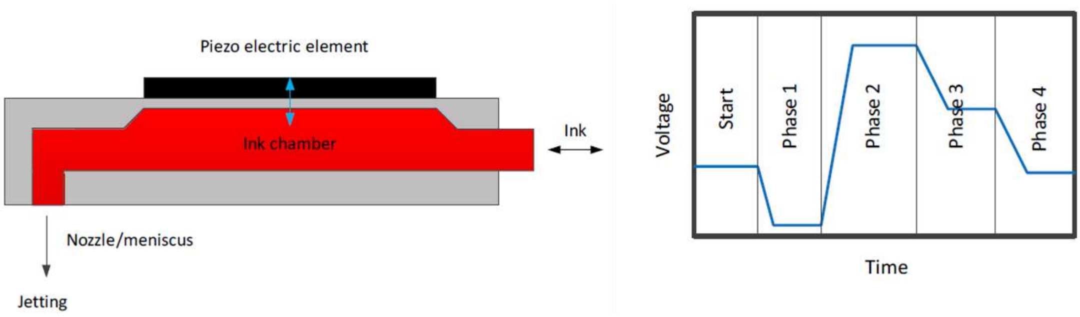

(a) (b)

Figure 1.3.3: schematic diagram of (a) piezoelectric print head and (b) firing voltage waveform. The initial negative segment refills the ink chamber with new ink, while the positive segment compresses it to generate a drop. The next sections bring the piezo and the chamber to the initial position.[40] *The shape of the waveform and the number of segments are highly dependent on ink formulation.*

Ejected droplets land on the substrate, wetting it to a degree which depends on the chemical affinity between ink and substrate and on the ink viscosity, then the drops dry by solvent evaporation.[41]

In order to have good droplet formation and detachment by the printhead, ink formulation is essential. Parameters like viscosity, surface tension, density and volatility must be adjusted to be in the printer working range, and even the gaseous content of the ink has to be accounted for. In addition, colloidal suspensions (like metal nanoparticles inks) should be ideally filtered to preserve the nozzles, which could be easily clogged.

The piezoelectric inkjet printer used for this thesis project will be described in detail in the Methods section.

2 Results and discussion

2.1 Experimental design

The object of this thesis is the development of a label free, *in situ* method for reaction imaging based on Raman spectroscopy within a microfluidic chip. By exploiting the high spatial resolution of the micro-Raman measurements, the devised system is potentially able to provide an exact image of all reaction phases, from the moment reactants start to mix until the product begins to form, ideally identifying eventual intermediates and showing the mechanism of the reaction through the evolution of bond vibrations. The low sensitivity of Raman measures is solved by using a solid-state gold nanoparticles substrate to enhance Raman signals, inkjet-printed at the bottom of the channel inside the chip. The investigated molecules are absorbed on the SERS substrate, creating a "spectral photography" of the reaction as it is occurring.

The experimental route followed to develop this microfluidic device and its operative protocol can be divided into three parts, as sketched in Figure 2.1.1. A first prototype, made of inkjet-printed glass and PDMS, was used to determine the right experimental setup, tested with three non-reacting dyes. A second design of the whole device was then produced according to the reaction characteristics, together with preliminary spectroscopic studies of all molecules involved. New channels geometry and device materials were implemented. This last chip was then used both to investigate the formation of a Schiff base and to follow two non-interacting dyes, with the aim of showing the real potential of the method and technology presented in this work.

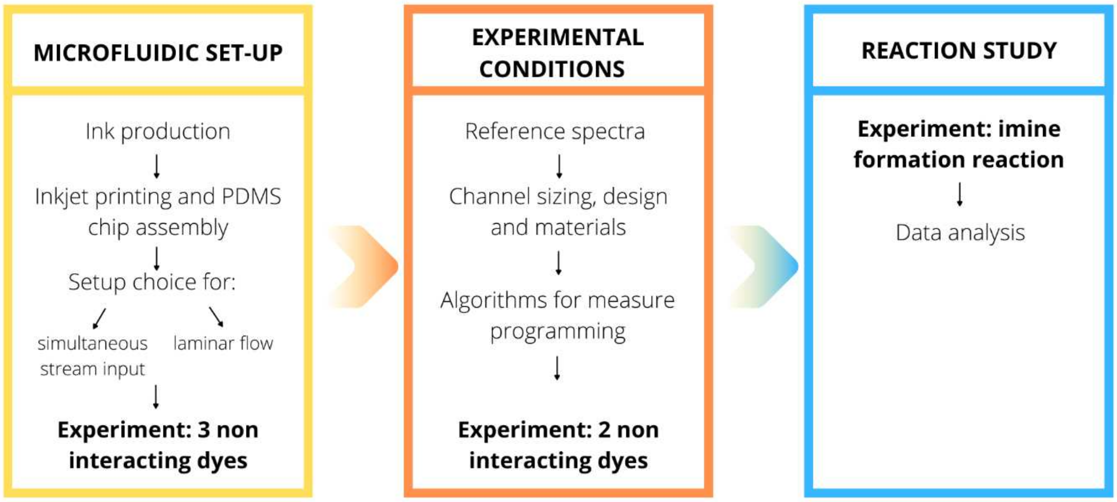

Figure 2.1.1: conceptual map of the experimental route followed in this work.

2.2 Characterization of Au nanoparticles ink and inkjet-printed substrate

The ink formulation was prepared by adding a PVA (polyvinyl alcohol) solution to a suspension of nanoparticles obtained by laser ablation, followed by multiple centrifugation steps to obtain the desired concentration. PVA is an additive needed to improve the stability of the gold colloid and prevent its aggregation during centrifugation and in the printhead nozzles during the printing process. After printing, the layer of PVA was removed with a thermal treatment, by heating the printed substrates to 500 °C for three hours under ambient atmosphere.

The ink production was monitored by UV-vis spectroscopy. The ink quality was ensured by checking that the Au nanoparticles did not underwent significant aggregation. This was done by comparing the UV-vis spectrum of the ink against that of the ablated particles: the two spectra (Figure 2.2.1) show an identical profile, with a redshift of the maximum. The latter can be attributed to two main causes. First, the mixing with the PVA causes a redshift due to the increase in the refractive index of the local environment around the nanoparticles. Second, the centrifugation steps have the consequence of discharging the smaller nanoparticle fraction, and the resulting larger particles are associated with a slightly red-shifted plasmonic band. The ink concentration (in Au nanoparticles) was determined to be $2.3\cdot10^{-8}$ M by estimating its molar extinction coefficient with Boundary Element Method simulations, following a previously published procedure.[42]

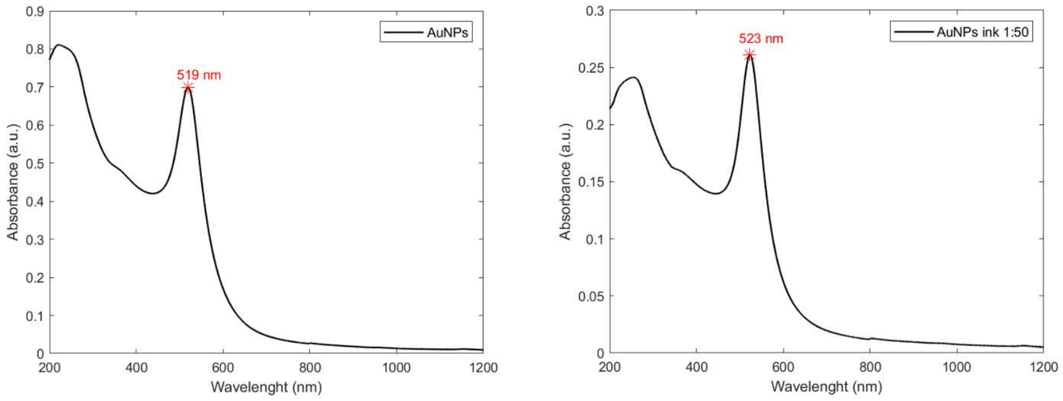

(a) (b)

Figure 2.2.1: absorbance spectra of the ablated NPs (a) and of the AuNPs_PVA ink (b). The maximum shifts from 519 nm to 523 nm.

The ink was used to print some circular spots of 1.5 mm in diameter to check the inkjet performance and for further SERS experiments. Figure 2.2.2 reports images of the latter, acquired at 20x magnification. The spots were inkjet-printed in three layers on a glass slide. Previous studies at the guesting lab had already verified that, using the same printing parameters and ink formulation, the printer ejects droplets with a diameter of around 25-30 μm, so a distance of 15 μm was chosen between two adjacent droplets to make them overlap.[43] The spots resulted compactly covered with ink, however with a noticeable coffee-ring effect. This is the name given to the phenomenon of ink concentration on the perimeter of the drop during solvent evaporation, caused by the capillary flow of the solvent within the droplet, which moves from the centre of the drop towards its pinned edge[44]. This effect can be limited by using a more hydrophobic substrate (for water-based inks), which leads to a reduction of the radius of the drop and less dispersion towards the edges, or by mixing solvents with different surface tension to influence the internal currents in the drop. As shown in picture (b) of Figure 2.2.2, printing multiple layers is another way of obtaining a good distribution of ink over all of the surface.

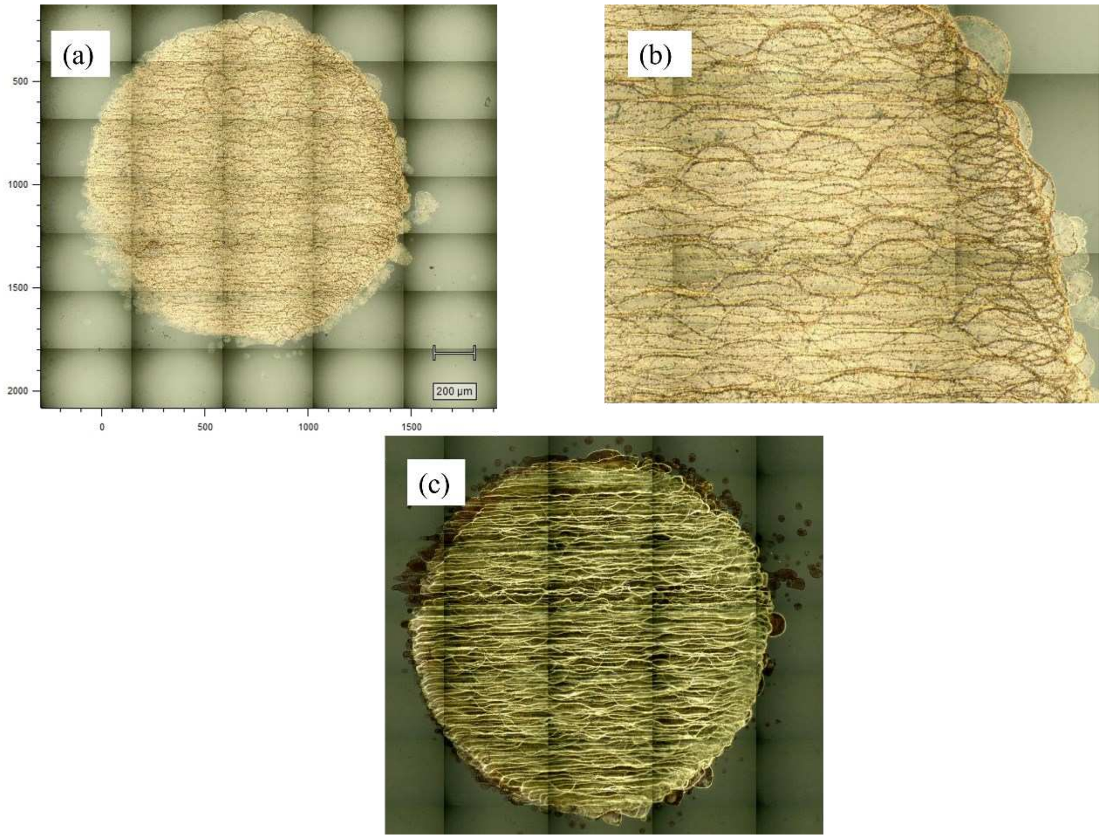

Figure 2.2.2: photos of a spot printed with AuNP ink on a glass substrate, with 3 layers and 15 µm of drop spacing, after thermal treatment. All the photos were taken with a 20x objective on the microscope of the Renishaw Raman spectrometer. (b) Is a magnification of (a), while (c) is a photo of a different spot taken upside-down, namely viewing it through the glass substrate, showing the layer of ink in contact with the glass slide.

The removal of PVA from the printed SERS substrate was verified by the absence of peaks on the Raman spectrum of the spots (Figure 2.2.3) after the thermal treatment at 500 °C for 3 hours, as expected by TG (thermogravimetric) and FTIR studies.[45]

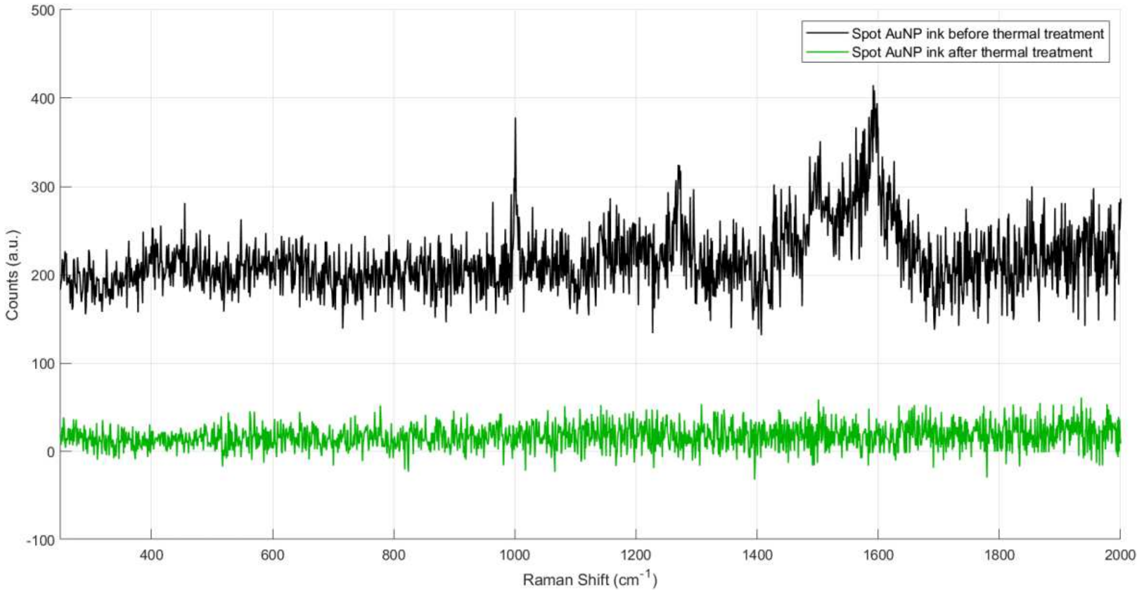

Figure 2.2.3: Raman spectra of inkjet-printed SERS substrate before and after thermal treatment, recorded with 633 nm laser, 10s acquisition time, 10x objective and 1 mW laser power.

2.3 Optimization of flow parameters within microfluidic chips

As already mentioned, the SERS analysis is configured as *label-free*. It implies the assumption that the first species passing over the substrate may be irreversibly adsorbed over it, so the worst scenario is the one in which the substrate is disposable. If not considered, it may even result in the so-called substrate memory effect, definitely detrimental for the overall measure and data analysis. it is therefore essential that all the reagents enter the microfluidic chip in laminar flow, without air bubbles, and at the same time. Preliminary studies about fluid dynamics were carried out using fluorescent and non-reacting dyes. Optimisation of the flow rate was necessary to avoid turbulent mixing and favour laminar flow, in which the reagents mix together more slowly and therefore over a longer path within the chip. The choice of using dyes allows laminar flows to be followed by both visual inspection (high concentration fluorescence emission) and SERS (low concentration) within a simple chip design.

The first chip prototype was then made by inkjet printing AuNPs in a pattern with three inlets and a straight channel on a glass slide (Figure 2.3.1a). The channel structure was made by PDMS following the procedure described in the Methods section, and solted to the printed glass with an O_2 plasma. This resulted in a chip with squared shaped channels with a 100 µm nominal height. The chip was then connected to the syringes with 0.3 mm internal diameter capillaries (Figure 2.3.1b).

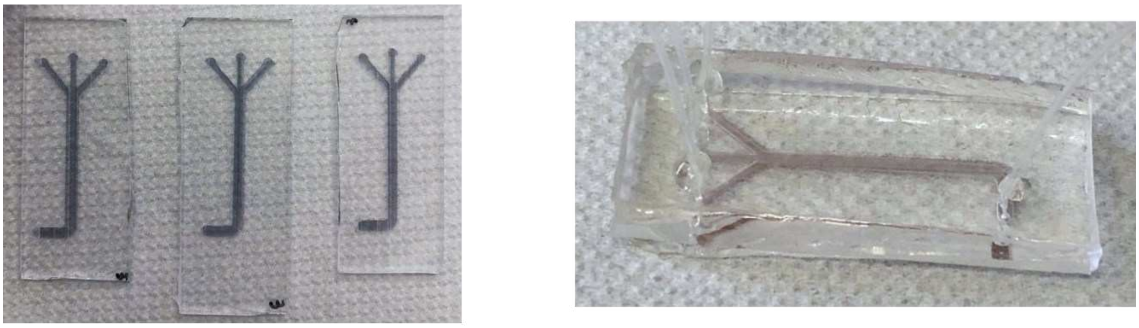

(a) (b)

Figure 2.3.1: (a) the inkjet-printed channel design before thermal treatment; (b) the assembled microfluidic chip.

A similar series of chips was also prepared in this way, but without printing the bottom of the channels with AuNPs. These were used to study a tri-component system of fluorescein and water, observing its behaviour at different flow conditions with a microscope operating in fluorescence (Figure 2.3.2).

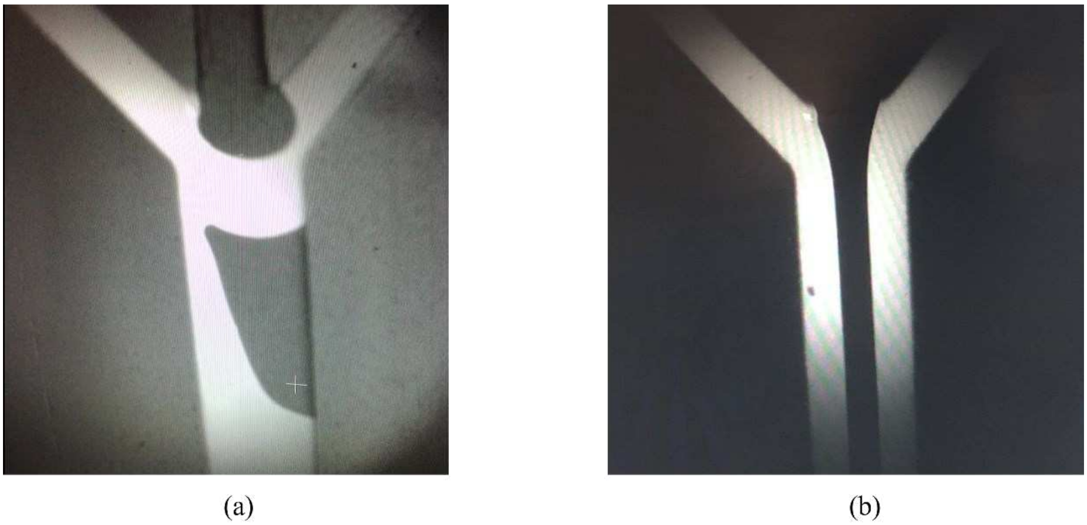
(a)
(b)

Figure 2.3.2: Fluorescein-water-fluorescein system in a three inlets PDMS microfluidic chip, observed under a 480 nm lamp. The bright flows correspond to the fluorescein thanks to its peculiar emission. (a) Air bubbles preventing laminar flow versus (b) laminar flow. In both condition the flow was set at 20 µL/min on all channels.

It was found that laminar flow can be established in a large range of flow velocities, from 1 µL/min to 100 µL/min.

As mentioned above, it was essential to optimize the input of all the three solutions in order to let them enter simultaneously and already under a laminar flow. As already discussed, the laminar flow can be easily established. The simultaneous input was instead addressed using a two pumps and three valves system, as sketched in Figure 2.3.3. For a chip with three inlets, two pumps were loaded with three syringes each, containing the molecules of interest and water, respectively. The six syringes were then connected to three *three-ways* valves, so that each valve could choose to output water or one of the reactants. Before the start of the experiment, water was pumped inside the chip to establish laminar flow at 15 µL/min, and after about five minutes the three valves were simultaneously switched to let the reactants flow into the device. Particular care was dedicated to make sure that no air bubbles were created when joining the different parts of the setup, as to not disrupt the laminar flow within the chip.

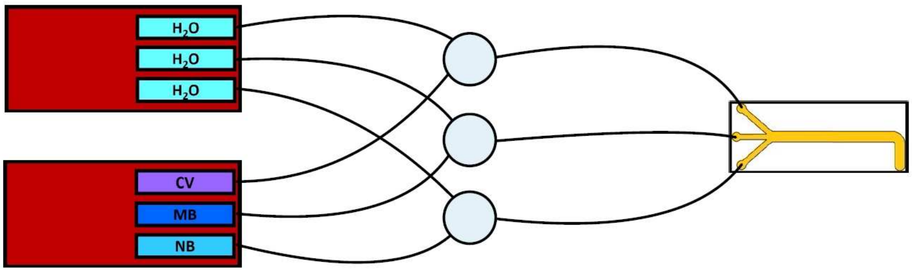

Figure 2.3.3: Schematic representation of the experimental setup for a chip with three inlets. In red are the two syringe pumps loaded with water and the molecules of interest, connected to the three valves. The outlets of the valves are connected to the microfluidic chip which is placed under the microscope of the spectrometer.

This experimental setup was tested by injecting 20 µM solutions of Crystal violet (CV), Methylene blue (MB) and Nile blue (NB) and by recording a 2D Raman map in correspondence of the crossing of the three input channels, with a 100 µm spatial resolution. Since PDMS has its own Raman spectrum, it was chosen to place the chip upside down, so with the glass side facing the instrument. The spectra were acquired across the glass slide with a 633 nm laser at about 1mW and with 5x magnification, 1s of acquisition time, and with the dyes flowing at 15 µL/min.

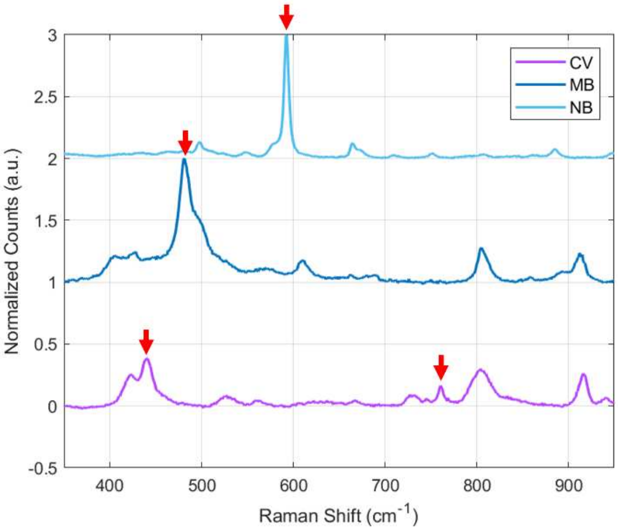

Figure 2.3.4: reference SERS spectra of the three dyes in the 350-950 cm^{-1} window, taken with the 633 nm laser, 10s acquisition time, 10x objective and 1mW laser power. The dyes were absorbed on inkjet-printed Au spots as in Figure 2.3.1. Red arrows mark the characteristic peaks of the dyes, respectively at 593 (NB), 481 (MB), 441 and 760 (CV) cm^{-1}.

To produce 2D µRaman maps, the instrument acquires Raman spectra at regular intervals along a grid manually located and spaced by the operator. The number of spectra acquired in this manner can be in the order of thousands, so semi-automated data analysis procedures must be employed in order to extract useful information. All these analyses were carried out by means of dedicated algorithms in the Matlab environment.

Two general approaches can be distinguished in data analysis. The first, called *univariate*, takes into account the intensity observed at a single Raman shift along all spectral datasets. The spatial distribution of the intensity at 760 cm^{-1} (Nile Blue) is reported in false-colours and superimposed on the photo of the chip (Fig. 2.3.5). This works very well for identifying substances with a very intense characteristic peak, like Nile blue in this case, but may fail whenever a spectrum has a low signal-to-noise ratio, even if it could be clearly recognized by looking at the overall spectral shape.

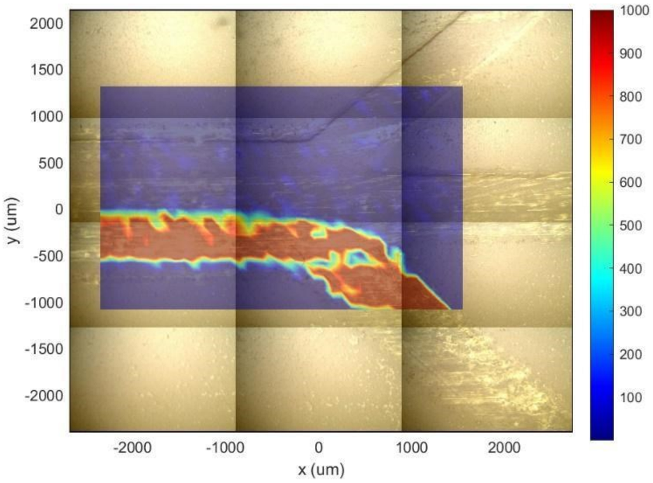

Figure 2.3.5: spatial distribution of the intensity at 593 cm^{-1}, characteristic peak of Nile blue.

The second main category of data analysis, called *multivariate*, takes into account multiple variables (i.e. more than a single intensity ad a specific frequency) to address spectral identification. Whenever reference spectra are available, one of the best choices consists in comparing the map spectra with the reference spectra of the dyes. The Pearson's R coefficient measures the linear correlation between them and assigns a score to each map spectrum, with better correlations receiving a higher score and vice versa. Superimposing the colormap of the R-scores over the chip image shows the spatial distribution of the scores inside the channel, with the three dyes easily identifiable (Fig. 2.3.6). Nile blue, in particular, showed high scoring spectra in all its section of the channel, while Methylene blue was the least accurately recognised.

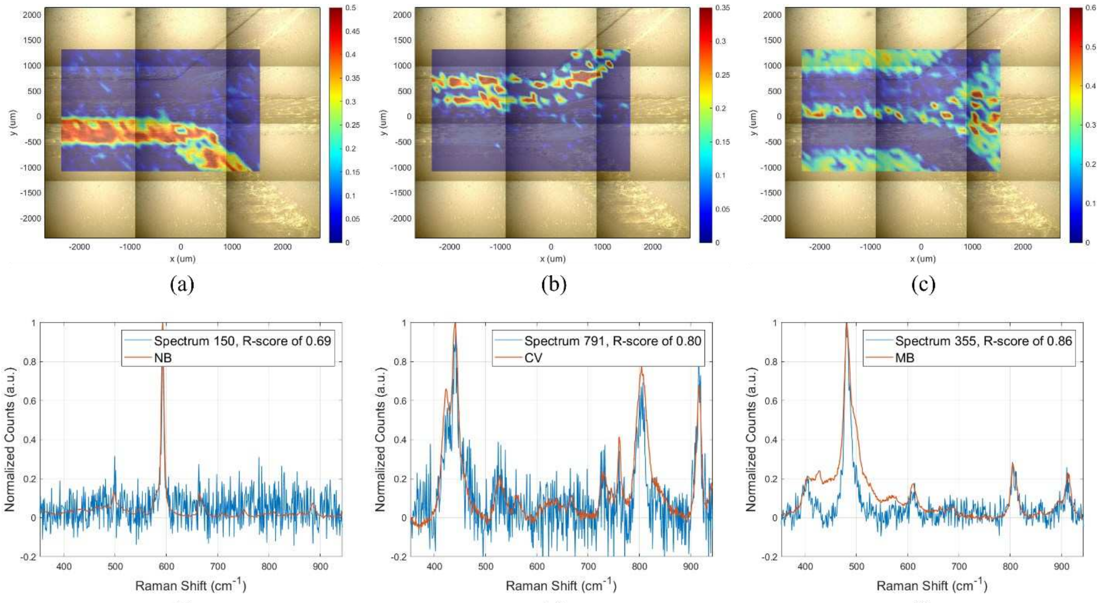

(a) (b) (c)

(d) (e) (f)

Figure 2.3.6: colour maps of the R-scores of the correlation between the recorded spectra and (a) Nile blue reference, (b) Crystal violet reference, (c) Methylene blue reference; (d,e,f) show the comparison between high scoring spectra of the experiment and their respective reference.

A second approach, still within the *multivariate analysis*, is best used when the spectra of different molecules aren't well distinguishable even by the means of reference spectra, or when they are superimposed. Principal Component Analysis (PCA) is a multivariate statistical analysis that can highlight similarities and differences in large datasets of samples. It takes the variables of the original data set (namely the intensities at each frequency) and computes their correlations to obtain a set of new independent variables, called Principal Components (PCs), along the direction of maximal variance in the dataset. It can be explained as if PCA expresses each spectrum as a linear combination having the PCs as the basis set and the PC-scores as the coefficients. In this way, each PC collects different spectral features, and every spectrum has a score associated to that PC, based on the weight that the specific spectral features of that PC have in it.

The PCs, also referred as *loadings*, may recall a real spectrum, but where both positive and negative intensities are allowed. Spectra with a positive score in one particular PC will contain peaks resembling the positive loadings of that PC, while spectra with a negative score will resemble the negative "peaks" of the loadings. Figure 2.3.7 reports the scores maps of PC 1,2 and 3 with the corresponding loadings for the microfluidic SERS analysis of the three dyes. These PCs clearly identify Nile blue (PC1, positive scores, Figure 2.3.7a and d), and Crystal violet (PC2, negative scores, Figure 2.3.7b and e), while again Methylene blue is less recognized but still visible in PC3 (positive scores, Figure 2.3.7c and f). A comparison of the loadings with the corresponding reference shows their correlation with the experimental peaks in the spectra. It is worth noting that Nile Blue can also be identified by positive scores in PC2.

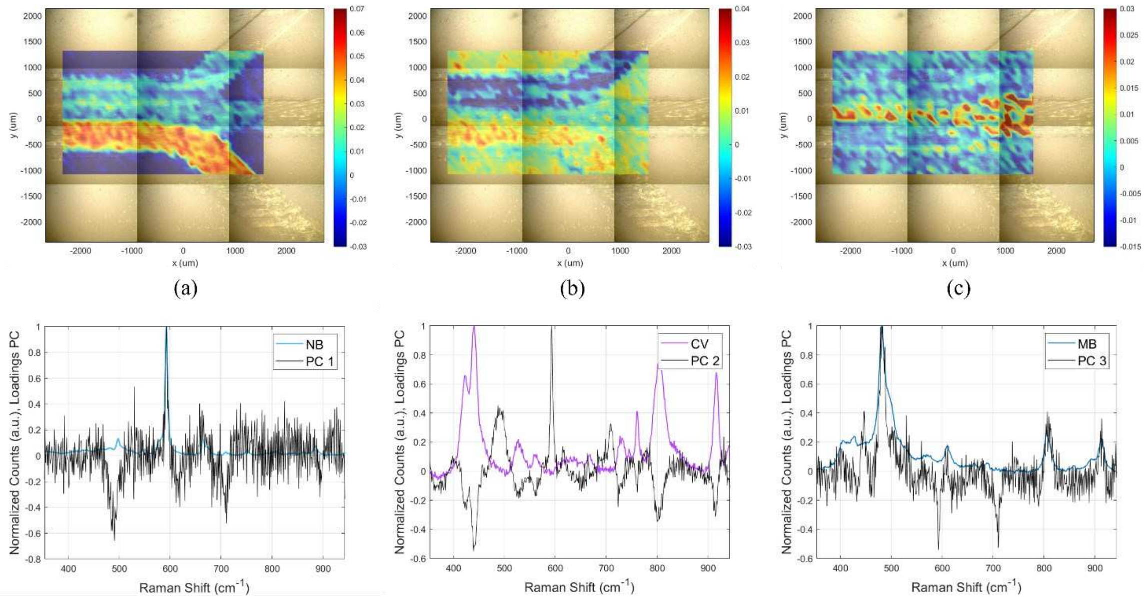

(a) (b) (c)

(d) (e) (f)

Figure 2.3.7: map of the PCs scores of (a) PC1, (b) PC2, (c) PC3. The corresponding loadings are reported in black in (d,e,f) against the reference spectra of the dyes.

Both the Pearson correlation analysis e PCA confirmed that the three dyes are distinguishable while flowing within the chip and that they enter at the junction of the three inlets with laminar flow, demonstrating the proper functioning of the experimental setup.

2.4 Determination of experimental conditions

The reaction chosen as the object of this study is the formation of a Schiff-base of pyridoxal phosphate from the reaction of pyridoxal 5'-phosphate (PLP, 1) with an aniline functionalized with a chelant (1,4,7-triazacyclononane, TACN) for Zn^{2+} cation (2).

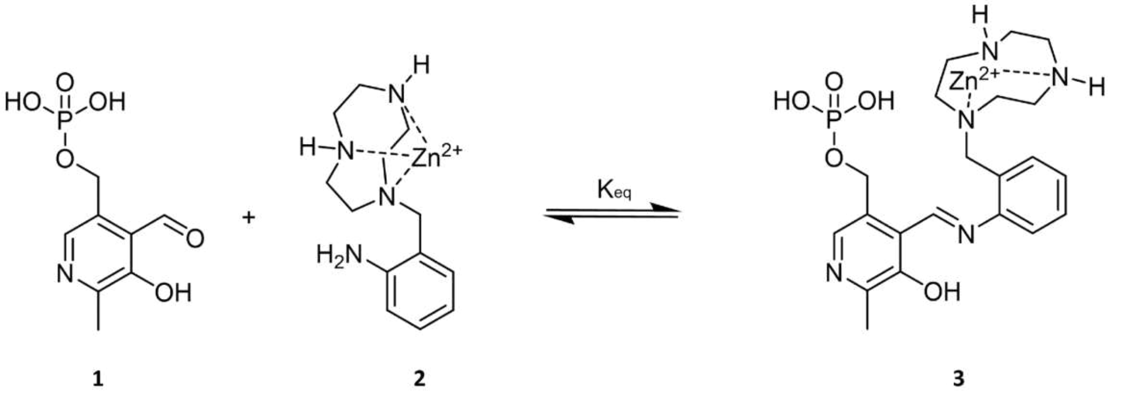

Figure 2.4.1: Formation of pyridoxal phosphate Schiff base

The mechanism of the Schiff-base formation proceeds through the nucleophilic attack of the amine on the carbon of the aldehyde group, producing an intermediate hemiaminal (or carbinolamine) that, after protonation by the solvent, loses a molecule of water to give an imine[46].

Pyridoxal 5'-phosphate is the biologically active form of vitamin B6 and it's one of the most ubiquitous cofactors found in nature, catalysing around 140 types of biochemical reactions, like transamination, phosphorylation and decarboxylation reactions.[47] The formation of imines between PLP and primary amines in aqueous solution has been known to the scientific community since the 1960s,[48] but most of the studies on this subject have been made with amino acids and aliphatic amines. Most protonated aliphatic amines have a pK_a of around 10.5 and are therefore protonated at pH 7, so the imine-forming reactions usually have to be carried out under basic conditions. However, basic pH catalyses the hydration of the aldehyde, limiting the imine formation. In contrast, protonated aniline has a pKa of 4.6,[49] allowing the reaction to occur at pH 7.

The reaction studied in the present thesis project involves an aromatic amine, that may take advantage of the resonance with the aromatic ring. Preliminary studies about the reaction of PLP and Aniline-TACN(Zn), provided by Luca Gabrielli's group with which we collaborate on this project, had already highlighted the fundamental role on the reaction kinetic and yield of both the TACN(Zn) group, by the aniline side, and the phosphate group, by PLP side. It was proved to come in a quantitative yield in 1 hour at room temperature at buffered neutral pH, while both lower yields and much longer reaction times are obtained if even only one between phosphate or TACN(Zn) is missing. In this context, the role of these two groups is going to be elucidated by the results presented along this thesis work.

2.4.1 Construction of reference library

The first step in analysing the reaction was finding out the best conditions to acquire the Raman spectra for both the reagents and the product. This addresses the double tasks of setting out the conditions for the subsequent µRaman analysis within the microfluidic chip, and of building a reference library to help with assignments of the same.

The first tries were made with a 633 nm laser source on gold nanoparticles substrates prepared by drop-casting deposition on a glass slide (Figure 2.4.4). The reactants and the product were separately casted over the spots in the concentration supposed to be used in the reaction within the chip (1 mM). Spectra obtained in this manner, however, had a low signal-to-noise ratio, with poorly defined peaks that were found not useful to distinguish between the three molecules. Further attempts made on inkjet-printed spots weren't more successful, even after trying to influence the absorption of the molecules on the substrate by changing the solution pH, or acquiring the spectra upside down to avoid fluorescence (data not shown). Raman spectra of the molecules in solid form were not useful as well because of their fluorescence.

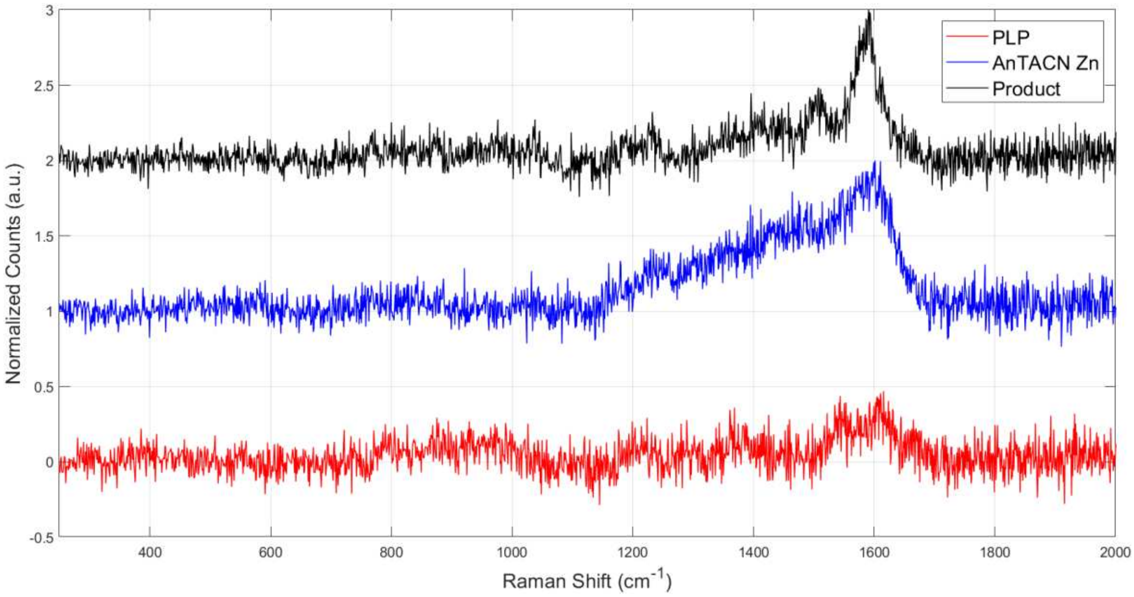

Figure 2.4.4: SERS spectra of the three molecules of interest taken on AuNPs drop castings, with the 633 nm laser, with 3 acquisitions of 10s, 10x objective and 1mW laser power.

A new attempt, still with the 633 nm laser, was finally successful. This time the molecules were mixed in a colloidal suspension of Au nanoparticles, and they produced spectra with well defined, and more importantly distinguishable, peaks (Figure 2.4.5).

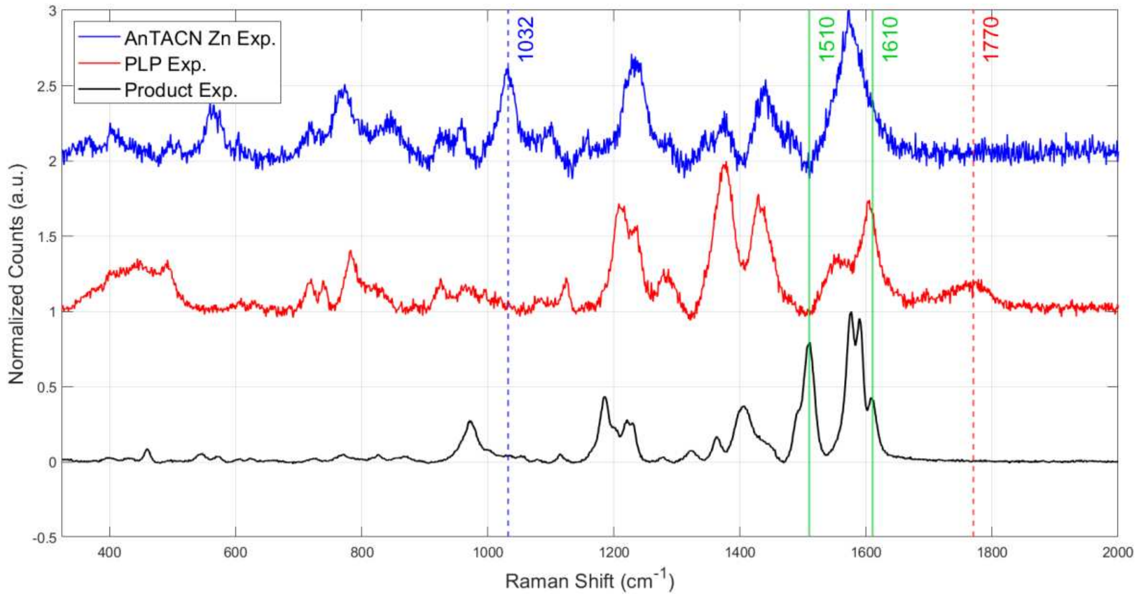

Figure 2.4.5: SERS spectra of the three molecules obtained with the colloidal AuNPs, with peaks diagnostic for the reaction underlined. The green lines show two peaks that only occur in the product (1510 and 1610 cm^{-1}), while the red and blue dotted lines show peaks belonging to PLP (1770 cm^{-1}) and Aniline-TACN(Zn) (1032 cm^{-1}) that disappear in the product spectrum. The spectra were acquired with the 633 nm laser, with 3 acquisitions of 30s,5x magnification and 5mW of laser power.

DFT simulations were run for the three molecules in order to provide a clear attribution of the most important, and characterizing, peaks. Details about the functional and the basis set used for the simulations may be found in the Methods section. A good correspondence between simulated and experimental spectra can be observed, where a reasonable frequency offset can be accepted. The proposed assignments are collected in the following tables, where the most intense and characterizing experimental bands are highlighted according to Figure 2.4.5.

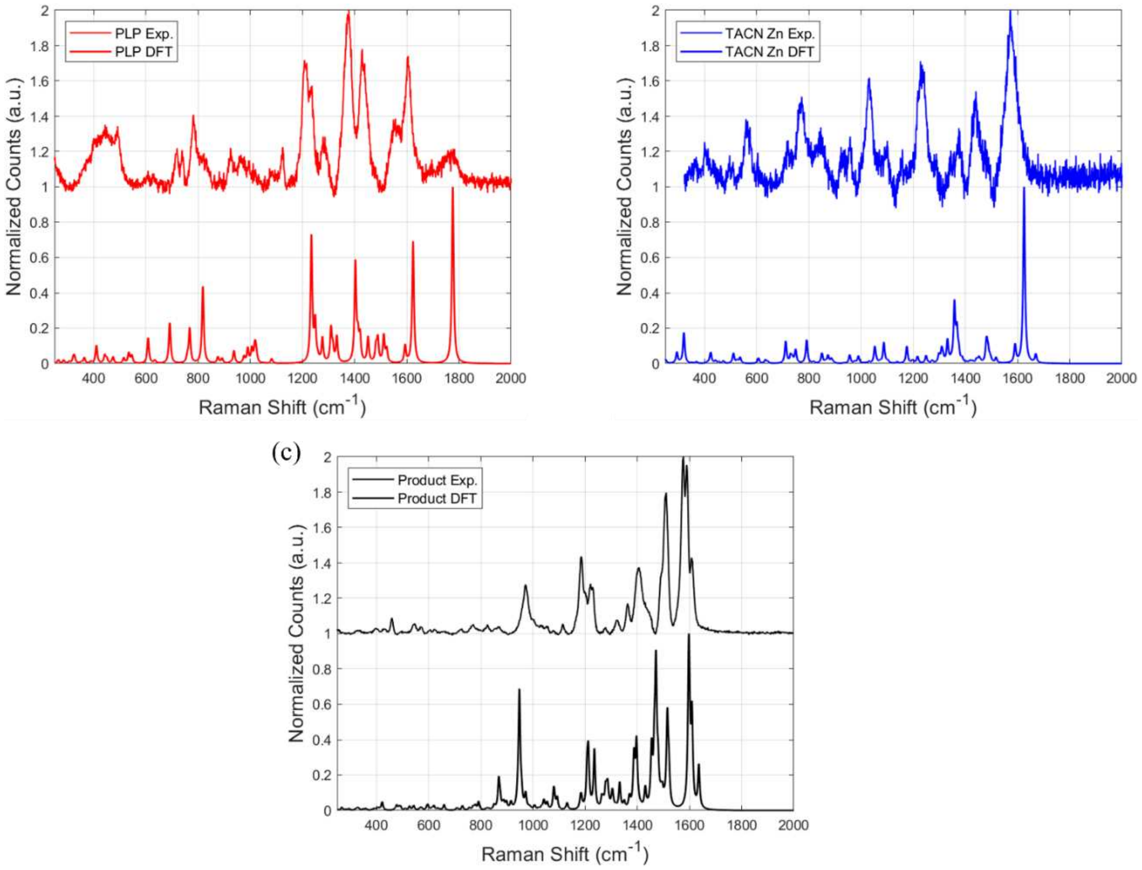

Figure 2.4.6: comparison of simulated and experimental spectra of PLP, Aniline-TACN(Zn) and the product. For each molecule, the bottom spectrum is the simulated one while the top spectrum is the experimental one.

Table 1: Proposed assignments of PLP vibrations.

Experimental	**DFT**	**Proposed Assignment**
1770 m/w	**1776 vs**	**C=O stretching**
1604 s	1624 s	Pyr ring stretching
1557 m	1593 w	Pyr ring stretching
1428 s	1421w	H—CO bending
1378 vs	1404 s	C—H_3 in phase bending
1286 m	1310 w	Pyr—H bending, P=O stretching
1279 m	1278 w	Pyr ring stretching, Pyr—O stretching
1233 s	1250 m	C—H_2 asymmetric bending
1209 s	1234 s	PyrO—H bending
996, 964 vw	1021, 1005 w	PO—H bending
926 w	936 w	C—H_3 in phase bending, Pyr—COH stretching
828 m	817 m	Pyr ring bending, P—O_4 stretching
781 m	768 m	Pyr ring stretching
739 w	693 m	Pyr ring planar deformations
444 m	442 vw	P—O_4 bending

** vs= very strong, s=strong, m=medium, w=weak, vw= very weak*

Table 2: Proposed assignments of Aniline-TACN(Zn) vibrations.

Experimental	**DFT**	**DFT Assignment**
1571 vs	1625 vs	Ar ring stretching, ArN—H_2 bending
1475 m	1483 w	C—H_2 scissoring (All)
1441 s	1443 vw	C—H_2 scissoring (TACN)
1379 m	1367 m	C—H_2 out of plane bending (All)
1342 w	1358 m	C—H_2 out of plane bending (All)
1288 w	1299 w	Ar—NH_2 stretching
1234 s	1251 vw	C—H_2 twisting (All)
1159 w	1176 w	Ar—H bending
1101 w	1088 w	N—H bending (TACN)

1032 s	**1053 w**	**ArN—H_2 twisting**
958,923 w	992,956 vw	C—H_2 out of plane bending, C-N bending (TACN)
846 m	851 vw	C—H_2 rocking
772 s	792 w	Ar—H, ArN—H_2 out of plane bending
720 m	711 w	ArN—H_2 out of plane bending
496 w	511 vw	Ar ring out of plane bending

Table 3: Proposed assignments of the product vibrations.

Experimental	**DFT**	**Proposed Assignment**
1608 m	**1636 m**	**C=N stretching**
1589 vs	1610 s	Ar ring stretching and C=N stretching
1577 vs	1597 vs	Pyr ring stretching and C=N stretching
1510 s	**1515 w**	**Ar ring stretching and C=N stretching**
1498 m	1472 vs	Ar—H bending
1440 w	1454 m	C—H_3 out of plane bending
1406 m, 1361 w	1396 m, 1387 m	C—H_2 bending (TACN)
1320 w	1333 w	Pyr—CN stretching
1279 w	1278 w	C—H_2 asymmetric bending
1230 m, 1221 m, 1114 vw	1233 s, 1183 w, 1131 w	Ar—H bending
1185 s	1210 m	Pyr stretching
1078 vw	1083 w	Pyr—CH_2—O stretching
1004 w	1006 vw	PyrC—H_2OPO_3 rocking
971 m	950 s	P—O_4 stretching
866 vw	874 m	TACN and Pyr collective stretching and bending modes

According to the assignments reported above, the diagnostic vibrations ascribed to the reagents are the carbonyl stretching in PLP (1770 cm^{-1}) and the amine bending in Aniline-TACN(Zn) (1032 cm^{-1}), which disappear when the new C=N bond forms in the Product, as expected. The new peaks appearing in the Product spectrum are instead attributed to stretching vibrations of C=N (1608 cm^{-1}, 1510 cm^{-1}).

2.4.2 Optimization of the channel design and Raman measuring setup for the reaction

The operating conditions required to have a simultaneous entrance of the reagents in the chip, and a laminar flow, were already found on a previous chapter on a simplified channel path. Since the aim is to run the amine formation between PLP and Aniline-TACN(Zn), the channels design has to be adapted to the new two-component system. It requires an internal volume compatible with the reaction time (1 hour), but still able to fit under the microscope of the spectrometer. Without considering the inlets, it was calculated that the main channel had to be 115 mm long, 2 mm wide and 500 μm high, with a serpentine shape to favour mixing of the reactants (Figure 2.4.2a, please refer to the Method section for details about the calculation). This allowed for a maximum flow of 1.9 μL/min in order to fit the reaction in the chip, which was lowered to 1.5 μL/min to make sure to capture the formation of the product within the chip. To ensure that the reactants would mix in the chip, an unprinted prototype (i.e. without AuNPs at the bottom of the channels) made of PDMS and glass was used to study the behaviour of water and fluorescein (Figure 2.4.2b). This revealed that mixing of the two streams started to visibly occur just after the first couple of turns in the channel.

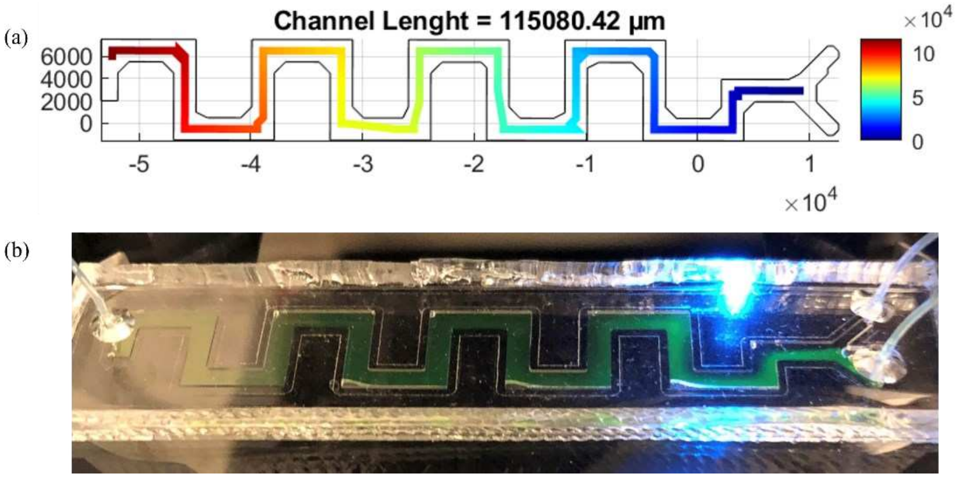

Figure 2.4.2: (a) channel length excluding the inlets and outlets and (b) mixing test with water and fluorescein under fluorescence microscope. A considerable degree of mixing can be seen with the naked eye already after the third bend.

The new chip was significantly bigger than the previous one, therefore a continuous rectangular µRaman map wasn't a viable option anymore, because it would have required the acquisition of a lot of irrelevant spectra and needlessly prolonged the experiment time. It can be roughly estimated that a continuous grid, larger enough to fit the whole chip (about 10x60mm) and 500µm spaced, requires 2800 spectra to be acquired, while recording only over the channel needs around half of that on the same resolution (about 1400 spectra mapping 115x2mm at 500µ resolution). To solve this issue, a Graphical User Interface was developed in Matlab. With this app, the user can superimpose the model image used for the inkjet printing with a photo of the chip taken by the microscope (which has known spatial coordinates). The two are adapted and properly superimposed by scaling, moving and rotating one in respect to the other. At this point, the app creates a grid with the chosen resolution only inside the perimeter of the model image. The spatial coordinates of each point of the grid are eventually stored in a file that can then be loaded on the spectrometer software in order to instruct it to collect spectra only over the channel and not outside. The appearance of the Matlab interface is reported in Figure 2.4.3.

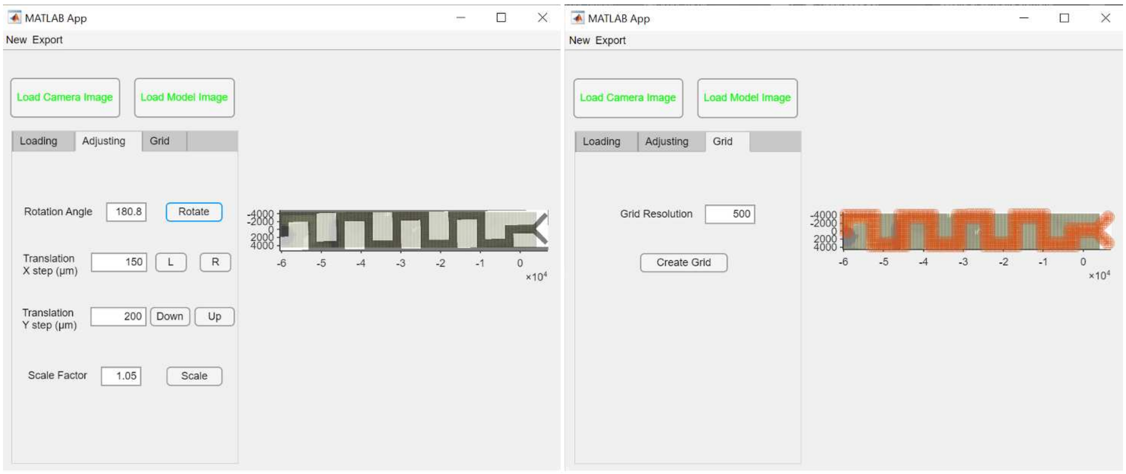

Rotation Angle 180.8

Translation X step (μm) 150

Translation Y step (μm) 200

Scale Factor 1.05

Grid Resolution 500

(a)

(b)

Figure 2.4.3: two screenshots of the Matlab app, (a) the section for adjusting the overlap of the two images, (b) the one for creating the grid.

2.4.3 New chip construction

The attempt made with the colloidal nanoparticles to obtain a reference library was successful (Figure 2.4.5), but the same approach couldn't be run within the microfluidic chip, as the reaction is supposed to follow its course unperturbed by the presence of colloidal nanoparticles. The inkjet printing of AuNPs on the bottom of the channel accounts exactly for this purpose, i.e. only a small fraction of the reactants and product will be absorbed and analysed, while the majority will flow unperturbed along the channel. Therefore, an optimized condition to acquire high quality spectra on a 2D SERS inkjet-printed substrate had to be found. Different laser lines were investigated on drop-casted gold nanoparticles. The 785 nm excitation wavelength produced a strong and broad band around 1400 cm^{-1} due to the photoluminescence of the glass substrate, making the original experiment setup, with the chip placed upside-down and the measure acquired through the glass, unusable. Nevertheless, once the glass problem was solved, the same excitation wavelength resulted in the spectra with the highest signal-to-noise ratio, so the excitation at 785 nm was preferred over excitation at 633 nm. This meant that the whole construction of the chip had to change. As already mentioned, the chip cannot be sampled from the top, because the laser beam would have necessarily passed through the PDMS, which would both attenuate its power and provide its own Raman signals. Using a fused quartz slide as the base of the chip, instead of glass, would have solved the problem, but unfortunately it wasn't available at the time. The chip was thus completely revised in terms of the materials and, consequently, the technologies needed to fabricate it. An aluminium foil, 1.5 mm thick, was used instead of the glass slide as the substrate for the inkjet-printed SERS substrate. A 500 µm thick sheet of brass, obtained via micro-milling by Doc. Ferraro's group with which we collaborated on this project, replaced PDMS for the channel side walls. It is worth noting that, in respect to PDMS, the caved brass framework is reusable, and does not have the well-known issue of molecular permeation that can sometimes happen with PDMS. As third, a 100 µm thick glass cover slide was used to close the chip at its top. The limited thickness of the cover slide, and the fact that the laser focus is hundreds of microns below, avoided the insurgence of the glass interference cited above. Finally, the three components were assembled with a silicone-based glue, while inlets ad outlets capillaries were inserted in sandblasted holes in the glass cover slide and attached with an epoxy glue. Figure 2.4.9 reports an image and a schematic representation of the chip.

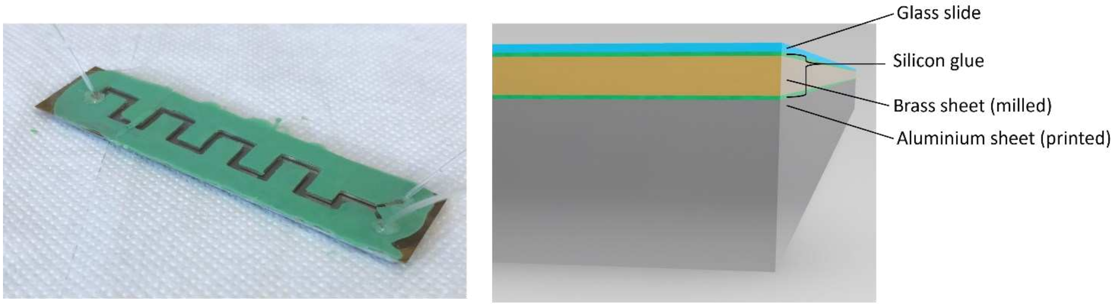

(a) (b)

Figure 2.4.9: (a) the assembled new chip; (b) schematic representation of the chip.

It should be noted that, despite the construction scheme of the new chip perfectly addressing all the prerequisites to acquire clear and intense SERS spectra, it is a substantially more fragile structure in respect to the standard PDMS chips, and it requires some practice in order to be properly assembled. Moreover, the channel hight is not perfectly controlled *a priori* anymore, because of the glue used to attach the chip components. Nevertheless, as it is going to be shown in the next chapter, none of these issues were found detrimental for the SERS measure within the microfluidic chip.

2.4.4 Mixing study

To verify the chip design and the experimental protocol developed above, Nile blue and Crystal violet were investigated with the new device. The experiment was run with a 633 nm laser at about 1mW laser power, with 10x magnification. The Raman map was set according to the Matlab App presented in Chapter 2.4.2 and acquired with a resolution of 500 µm, for a total of 1259 spectra with acquisition times of 1s each.

Figure 2.4.10: second iteration of the chip, photo taken right after running the experiment with the dyes.

As can be seen in Figure 2.4.10, a leak at the end of the chip caused the glass to fog up, so the last two turns of the channel are going to be excluded from the following analysis.

As previously mentioned, multivariate analysis is particularly useful when attributions driven by inspecting a single frequency may result in poor resolution between background noise and proper signals, even if of low intensities. For this reason, Principal Component Analysis was used to analyse the present µRaman map. The scores obtained on each spectrum for the first two principal components (PCs) are represented as false coloured map and superimposed to the optical image of the chip in Figure 2.4.11a and b, together with the loadings corresponding the same PC.

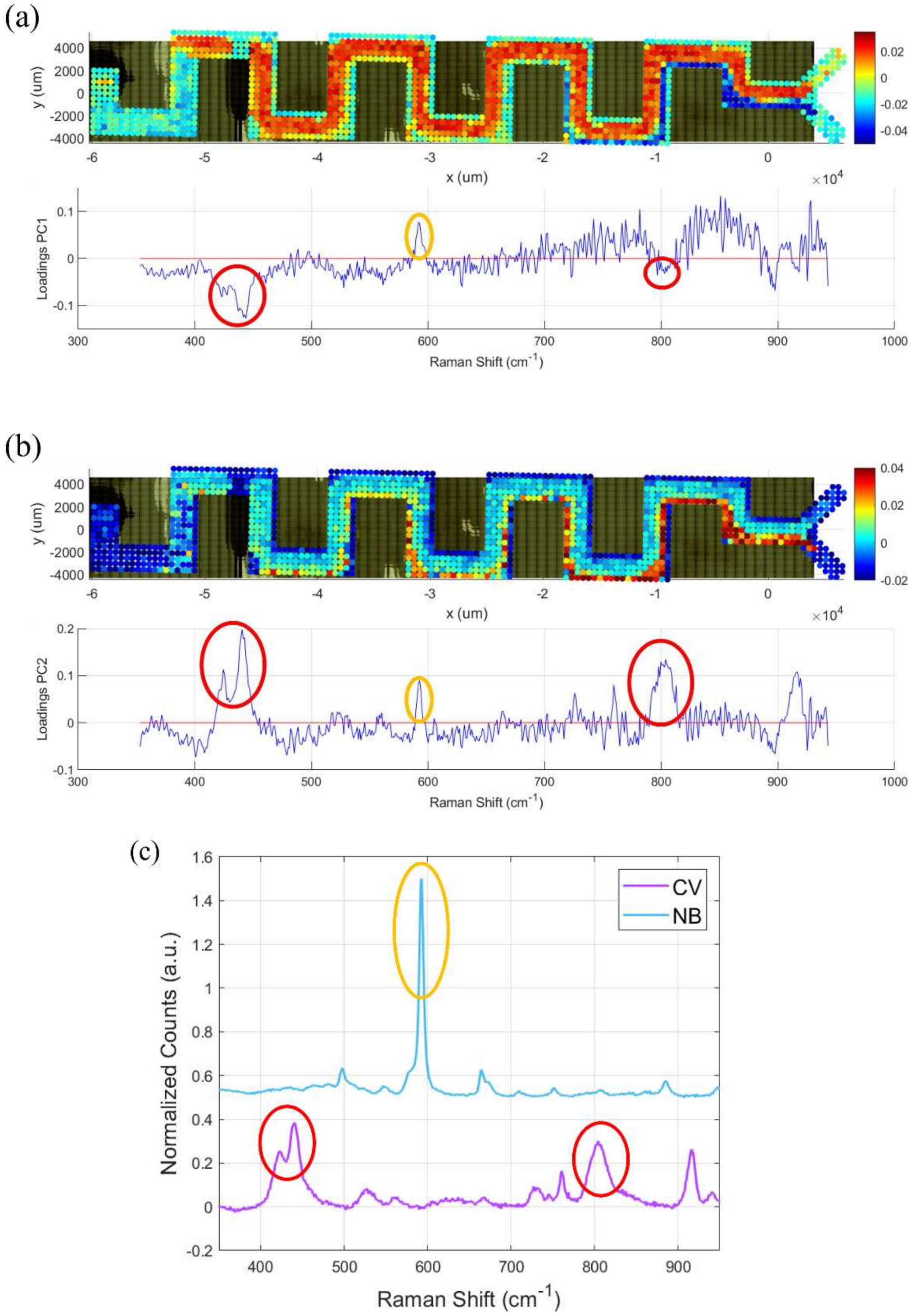

Figure 2.4.11: PC1 (a) and PC2 (b), with the scores map on top and the loadings on the bottom. (c) Normalized reference spectra of Crystal violet and Nile blue, taken with the 633 nm laser, 10s acquisition time, 10x objective and 0.1mW laser power. Highlighted in red and yellow are the characteristic peaks of Crystal violet and Nile blue, respectively.

The scores map of PC1 and PC2 show very clearly the flows of the two dyes inside the channel in Figure 2.5.2a and b. The red circles in Figure 2.4.11 highlight the most characterizing band for Crystal violet (CV), while the yellow circles do the same for the Nile blue (NB) dye. PC1 identifies NB with positive scores and CV with negative scores, while PC2 has spectral contributions of both dyes in the positive side of the loadings. However, it can be appreciated that CV has a higher contribution on PC2, as seen from the higher loadings of the corresponding peaks, so it is represented on the map by the highest scores. On the other hand, NB contributes less, so it's represented by scores between 0 and 0.01. As shown in the scores maps, the two dyes initially flow inside the chip with two well distinct streams, but quickly start mixing together, with the signals from NB dominating on CV.

An identical behaviour is depicted in the R-scores map of Pearson correlation, where the stream of Crystal violet can clearly be seen getting thinner and more confined to the side of the chip as mixing progresses, with the signals of Nile blue covering it.

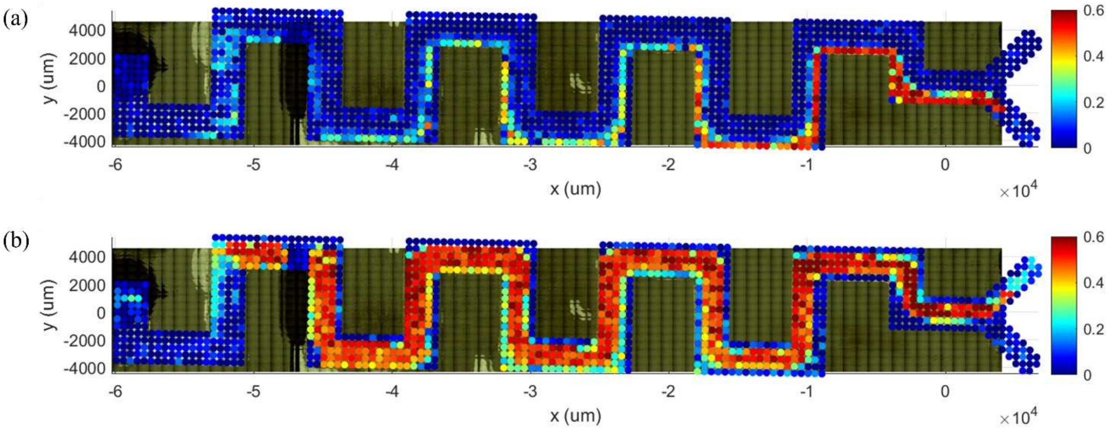

Figure 2.4.12: colour maps of the R-scores of the correlation between the recorded spectra and (a) Crystal violet reference and (b) Nile blue reference.

Further proof of mixing can be seen in figure 2.4.13, which depicts a scatter plot that combines the positive correlation scores of the two dyes. In this graph some points, for example the one highlighted in green, have high correlation scores with both NB and CV, which means that both references are recognized in the same spectrum.

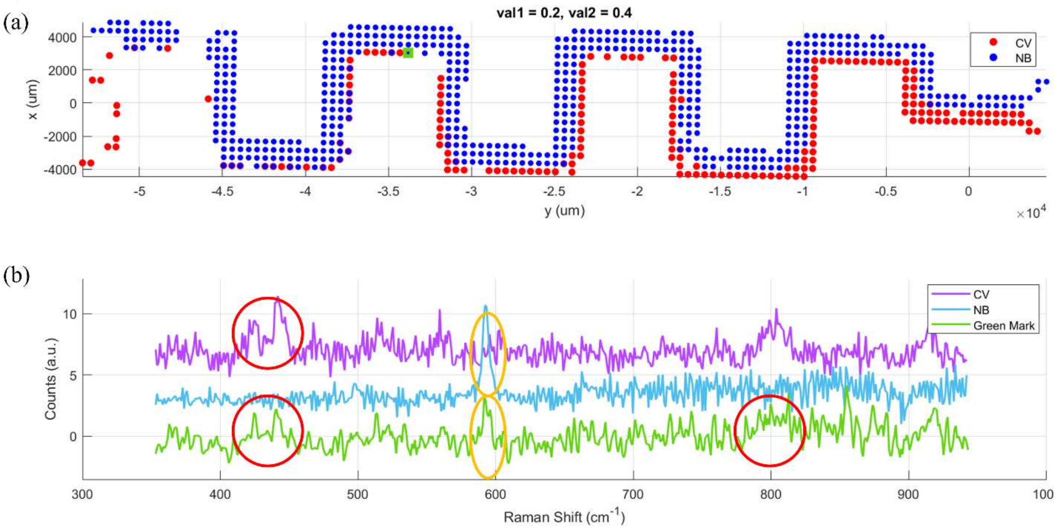

Figure 2.4.13: (a) scatter plot of spectra with correlation scores higher than 0.2 for Crystal violet and higher than 0.4 for Nile blue; (b) spectrum of the point highlighted in green compared to the reference spectra of Crystal violet and Nile blue: it contains the characteristic peaks of both of the dyes.

Another experiment was run on the same chip and with the same experimental conditions, but the map was acquired with a resolution of 250 μm. Figure 2.4.14 shows the spatial distribution of the scattering intensity at wavenumber fixed on the characteristic peak of Nile blue, 593 cm^{-1}: the colour gradient clearly displays the progressive diffusion of Nile blue towards the centre of the channel. This demonstrates the high resolutions achievable with Raman imaging, which theoretically is only limited by the choice of laser wavelength and the numerical aperture of the microscope objective.

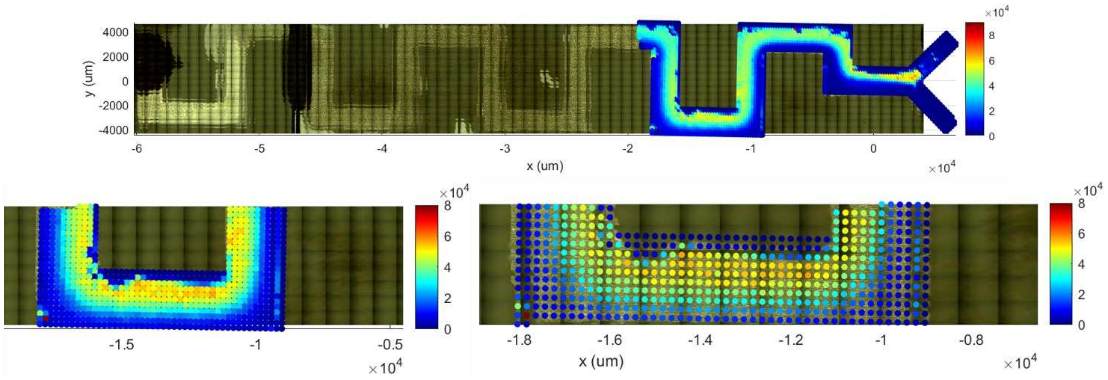

Figure 2.4.14: map of the intensity at 593 cm^{-1} with some enlargements.

2.5 Reaction Study

2.5.1 Microfluidic experiments results

The microfluidic experiment was carried out with a 785 nm laser at 50mW of power, on the brass chip. The spectrometer acquired a Raman map with a resolution of 500 µm, for a total of 1250 spectra with acquisition times of 10 s for each. The Raman map was set to recover spectra only in correspondence of the channels, thanks to the Matlab App presented in Chapter 2.4.2. Reagents were pumped in the chip with a syringe pump at 1.5 µL/min, while water was previously used to establish laminar flow, according to the scheme reported in Chapter 2.3 and schematized in Figure 2.3.3.

The interpretation of the Raman map required extensive usage of multivariate models, due to the complexity of the system and the multiple components present in the same. It must be recalled that the silicone glue, the epoxy glue and even the glass cover slide are sampled as well. PCA, together with the superimposition of the chip image obtained by the microscope equipped to the Raman instrument, was found to be the method that gave more promising results and could identify all the components of the system. The results are going to be presented according to the order of the principal components that were found best representing each component of the chip.

Figure 2.5.1a reports a false coloured Raman map of the chip according to the scores on PC1. It can be observed a clear expression of negative scores at the boundaries of the channel, marked with the green circles. By looking at the relative loadings plot and few selected spectra (Figure 2.5.1b), one may attribute the negative scores of PC1 to the silicone glue used to merge the chip components, which slightly protruded from the chip walls. The areas marked by purple circles in Figure 2.5.1a are instead ascribed to the glass cover slide, as one may appreciate by the relative traces in Figure 2.5.1b. The reason for such topical appearance of the glass band at about 1400 cm^{-1} may be ascribed to the imperfect positioning of the chip, which can result in the upper cover slide coming partially in focus in some areas.

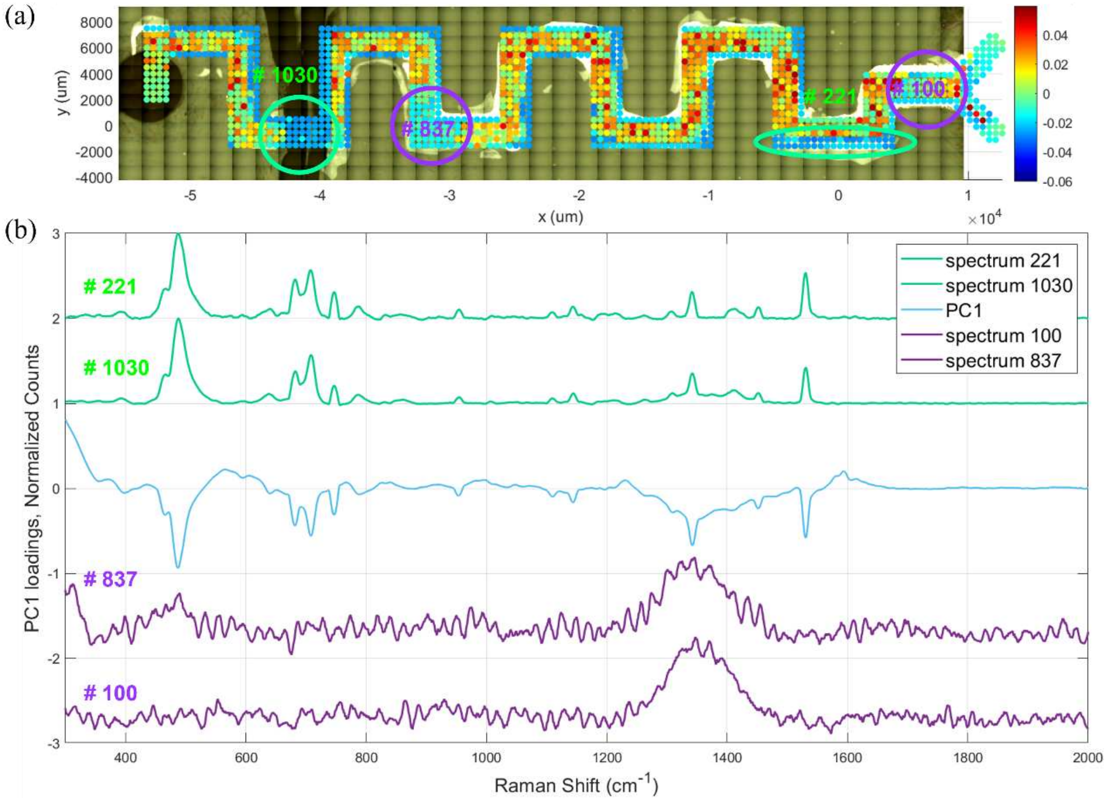

Figure 2.5.1: Score map (a) and loadings (b) from PC1, compared to selected spectra with a negative score. The spectra in purple are extracted from the corresponding zones marked in the chip and show just a prominent peak around 1400 cm^{-1}, ascribable to glass. The spectra in green, selected from the zones marked with the green circles, belong to the silicone-based glue. PC1 shows similar peaks in the negative loadings.

PC2 and PC4 distinguish between the silicon glue and the epoxy glue, assigning them opposite scores (Figure 2.5.2).

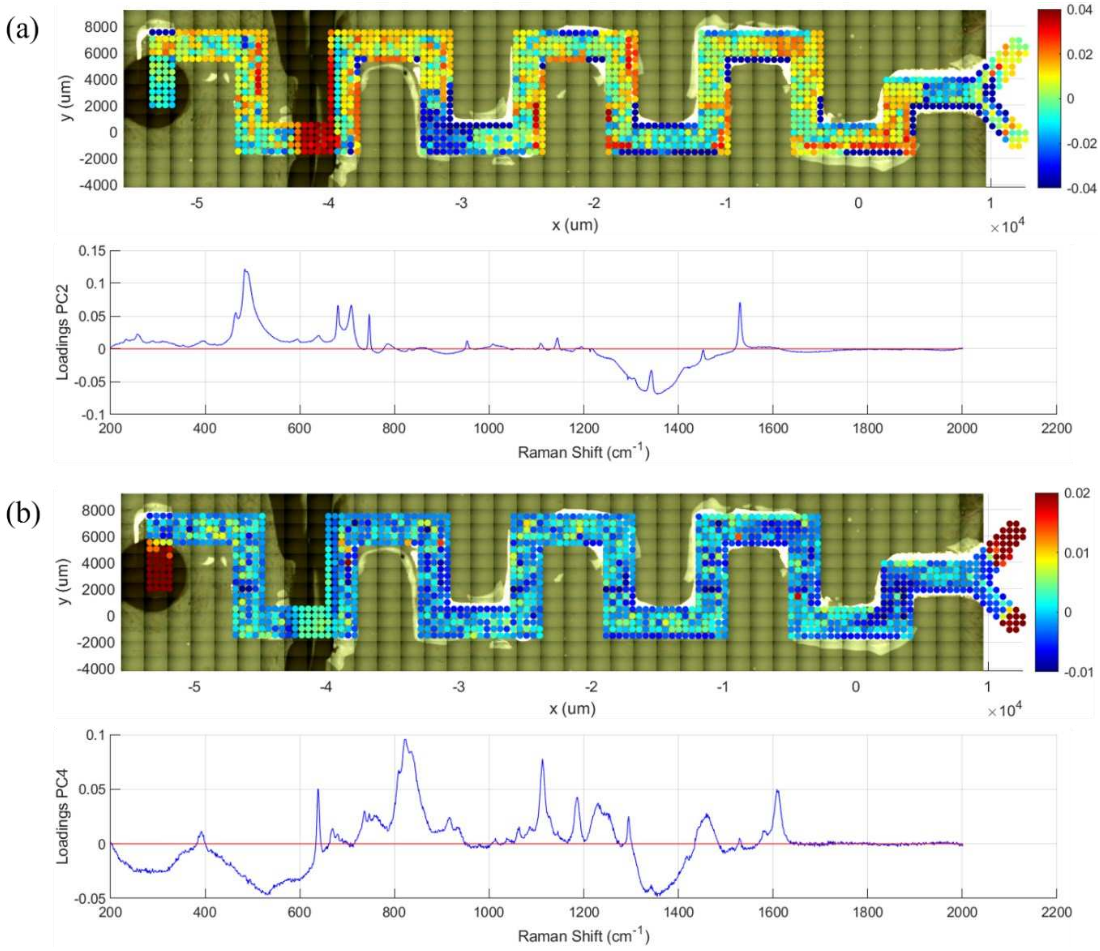

Figure 2.5.2: Scores map (top) and PC loadings for PC2 and PC4. PC2 (a) identifies the silicon glue with the positive scores (a vertical line of silicon glue was used to close two of glass cover slides to make the top of the chip).

The peaks of the reagents and the product could be identified in the loadings of PC6, PC8 and PC9.

Figure 2.5.3a reports a false coloured Raman map of the chip according to the scores on PC6. The relative loadings are stacked for comparison with the PLP, Aniline-TACN(Zn) and the Product reference spectra in Figure 2.5.3b.

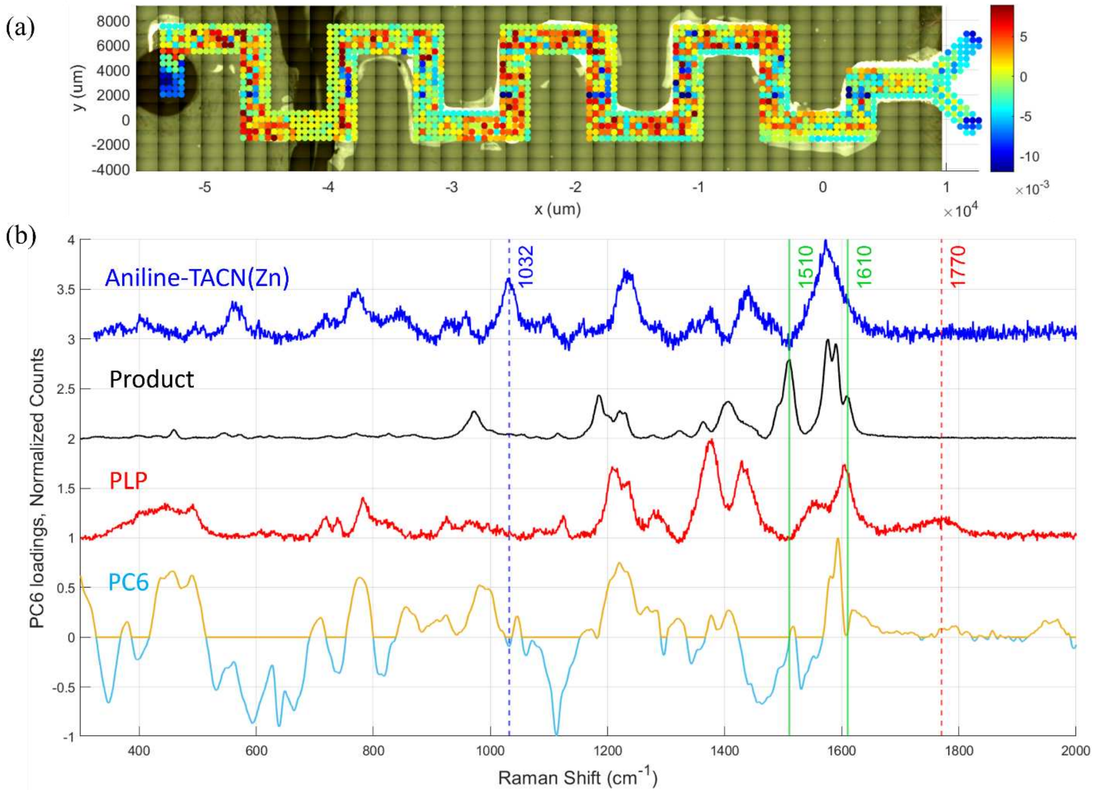

Figure 2.5.3: PC6 (a) scores map and (b) loadings compared to the three reference spectra acquired with the colloidal AuNPs. The positive loadings contain a peak at 1780 cm^{-1}, associated with PLP.

The positive loadings of PC6 reports signals that closely resemble the reference spectrum of PLP (Figure 2.5.3b): one may especially appreciate the doublets at about 1600cm^{-1} and at 1400cm^{-1} and the band at 1200cm^{-1}. Moreover, a contribution at about 1770cm^{-1}, ascribed to the COOH group, may be also noticed. On the contrary, the most characterizing signals for both Aniline-TACN(Zn) and the Product have loadings close to zero in PC6, meaning that these bands are not represented along this component.

The partial spectral overlap between all the three molecules especially at 1200 cm^{-1} and 1600cm^{-1} explains why some positively scoring spectra can be found at the end of the channel in Figure 2.4.12a as well, even if most of their spatial distribution is concentrated in the first part of the chip, as expected.

The PC6 scores trend along the channel is represented in Figure 2.5.4, where the PC6 scores are mediated for each spectrum on a channel section at different distances from the inlets. The overall trend appears constant along the channel length. Nevertheless, one must recall that several bands along the PC6 loadings may be ascribed to both PLP, Aniline-TACN(Zn) and the Product, thus making this PC ineffective in tracing a single species.

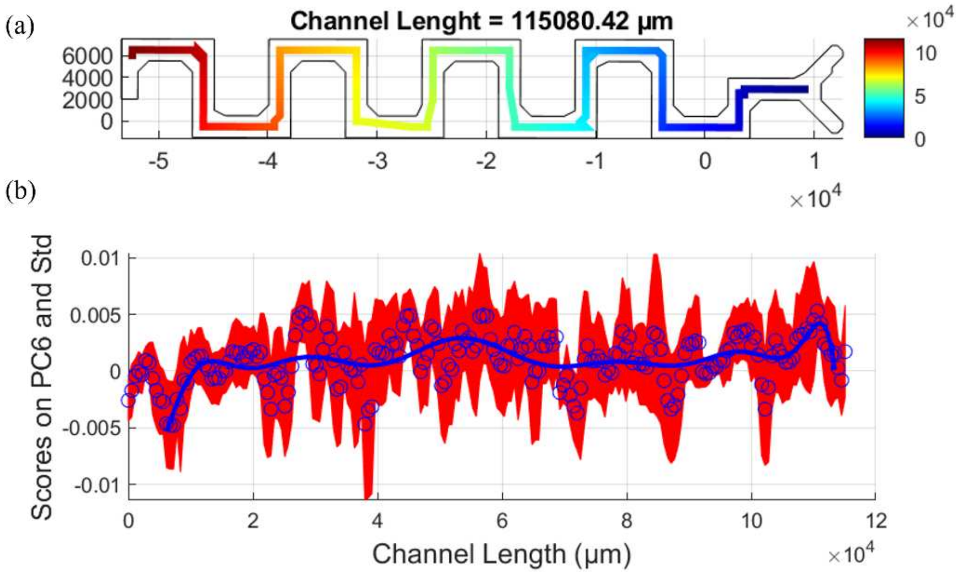

Figure 2.5.4: (a) channel length; (b) scores trend of PC6 with respect to channel length. Blue circles represent the medium scores in the corresponding channel section, with the blue line interpolating them, while the red area is the scores standard deviation.

PC8 contains spectral contributions ascribable to Aniline-TACN(Zn) on the positive loadings, especially around 1470, 1126 and 1060 cm^{-1}, while the negative loadings can better represent the peaks of the Product in the range between 1500 and 1600 cm^{-1} (Figure 2.5.5b). The spatial distribution of the scores of PC8, from Figure 2.5.5a indicates a progressive transition from positive to negative scores along the channel, coherent with reagents concentration decreasing and product appearance.

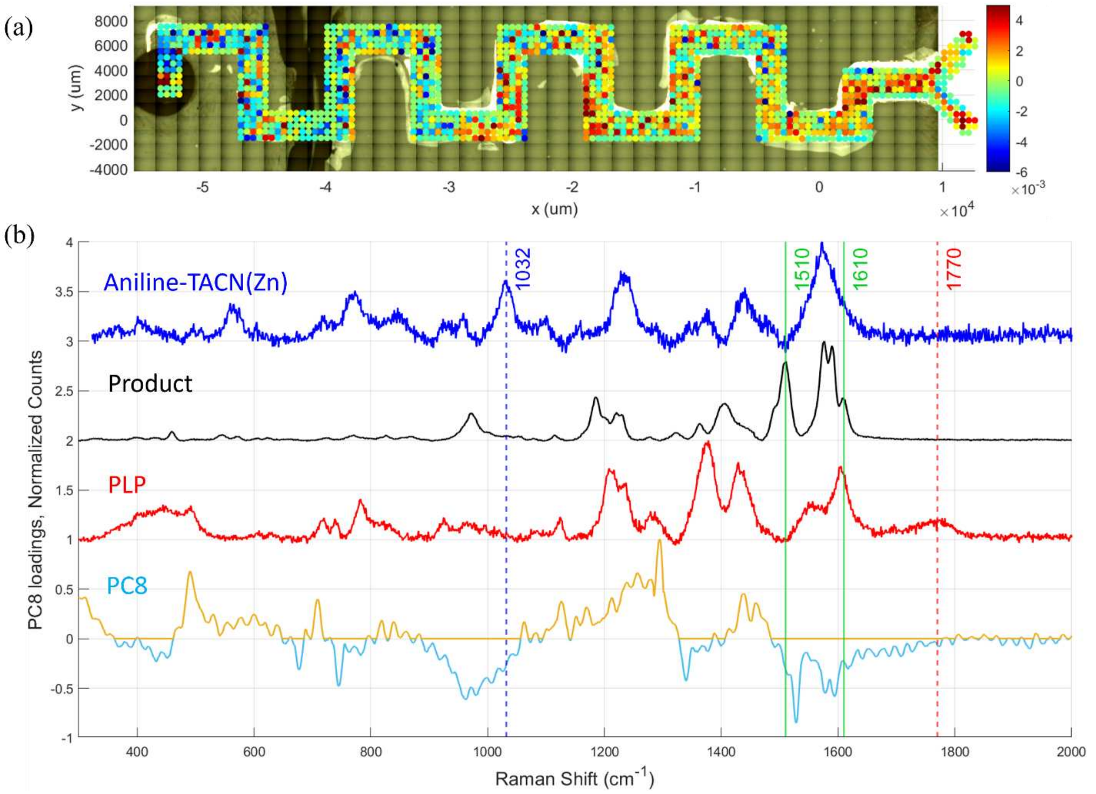

Figure 2.5.5: PC8 (a) scores map and (b) loadings compared to the three reference spectra acquired with the colloidal AuNPs. In the positive loadings the peak at 1060 cm^{-1} can be attributed to Aniline-TACN(Zn), while the negative loadings contain peaks at 1519 and 1618 cm^{-1} that can be associated with the Product.

The analysis of the scores trend along the chip length (Figure 2.5.6) confirms what already observed on the false-coloured map of Figure 2.5.5a, with the PC8 positive scores (attributed to Aniline-TACN(Zn)) decreasing towards the middle of the channel up to gradually higher negative values, attributed to the Product.

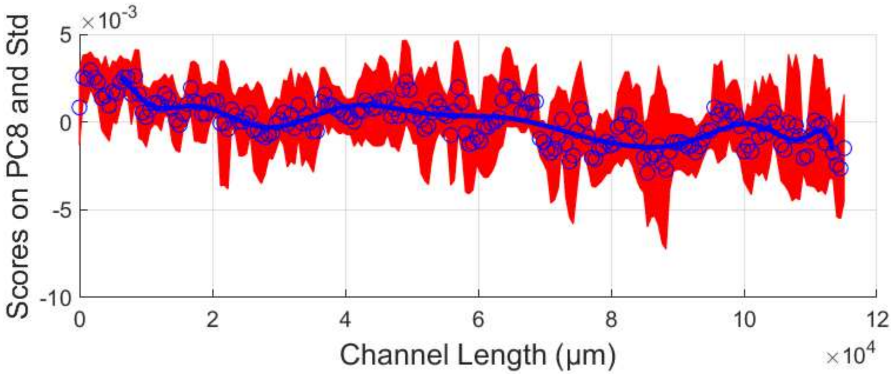

Figure 2.5.6: scores trend of PC8 with respect to channel length: the positive scores associated with aniline-TACN(Zn) start to go down in the middle of the channel.

Finally, from Figure 2.5.7b one may appreciate that the positive loadings of PC9 also contain spectral contributions of the Product, with peaks at 1515 and 1609 cm^{-1}, while the characteristic peaks of the reagents are absent. In this case, from both the false-coloured map of Figure 2.5.7a and the score trend of Figure 2.5.8, it is clear how the highest scores appear towards the end of the channel.

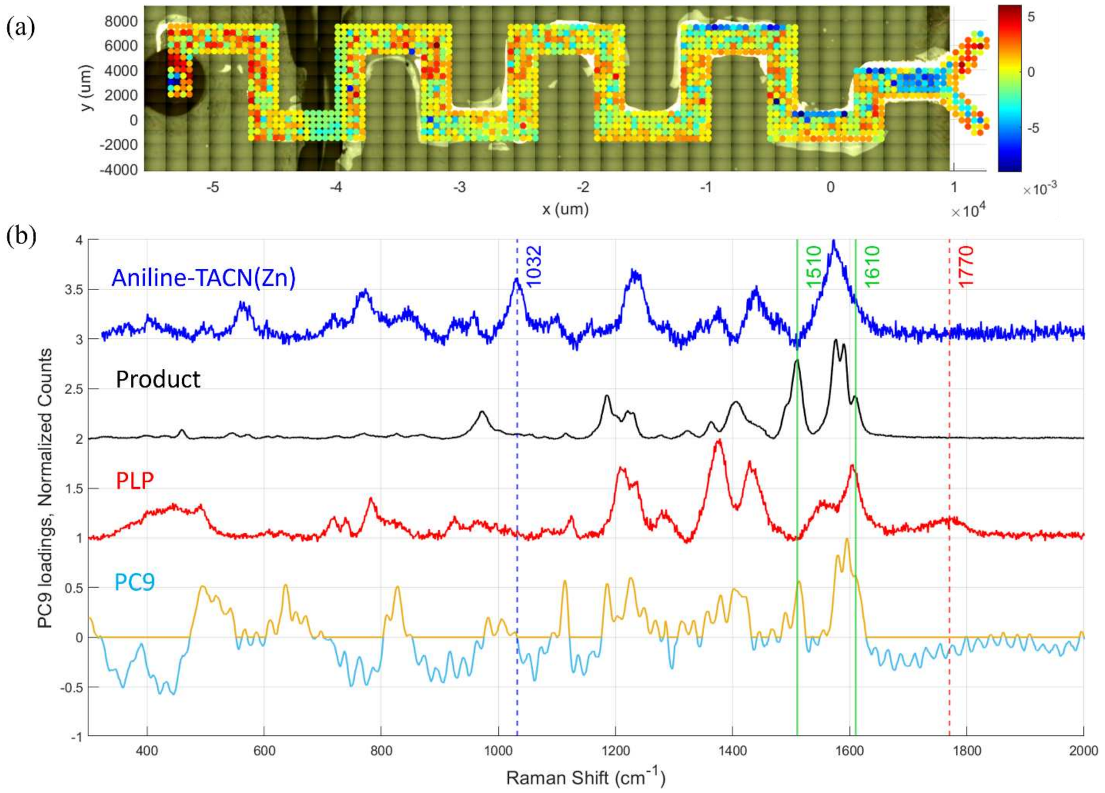

Figure 2.5.7: PC9 (a) scores map and (b) loadings compared to the three reference spectra acquired with the colloidal AuNPs. In the positive loadings the peaks at 1519 and 1618 cm^{-1} can be associated with the product.

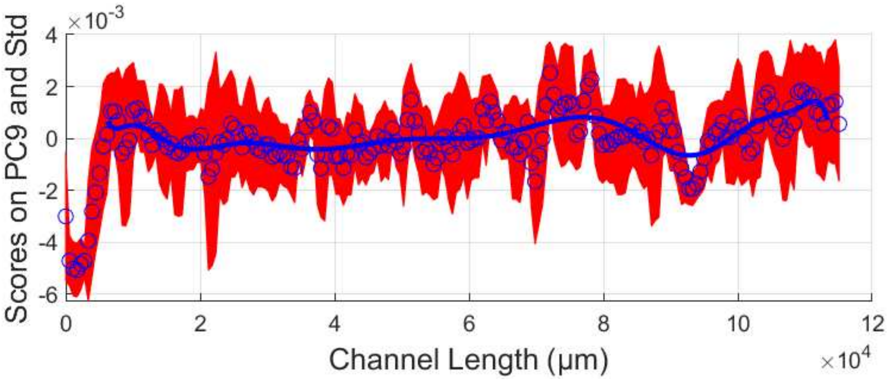

Figure 2.5.8: scores trend of PC9 with respect to channel length: the positive scores associated with the product start to increase towards the end of the channel.

The same should be read as a gradually increasing contribution of the bands ascribed to the Product, therefore its concentration, towards the end of the chip. The local drop of PC9 scores, at about 9 cm in channel length, can be well explained by the presence of the silicone glue located at about -4 cm on the x-axis in Figure 2.5.7.

As a final confirmation that the reaction inside the chip actually formed the imine product quantitatively, an ^{1}H-NMR experiment was run on the first aliquot of solution coming out of the outlet. The peak at 8.8 ppm is ascribed to the proton of the carbon involved in the C=N bond. The ultimate confirmation of the imine formation is indeed the absence of any peaks at around 10 ppm, that would have been characteristic of the presence of an aldehyde in the crude reaction mixture. Figure 2.5.9 shows the attribution of the most important peaks.

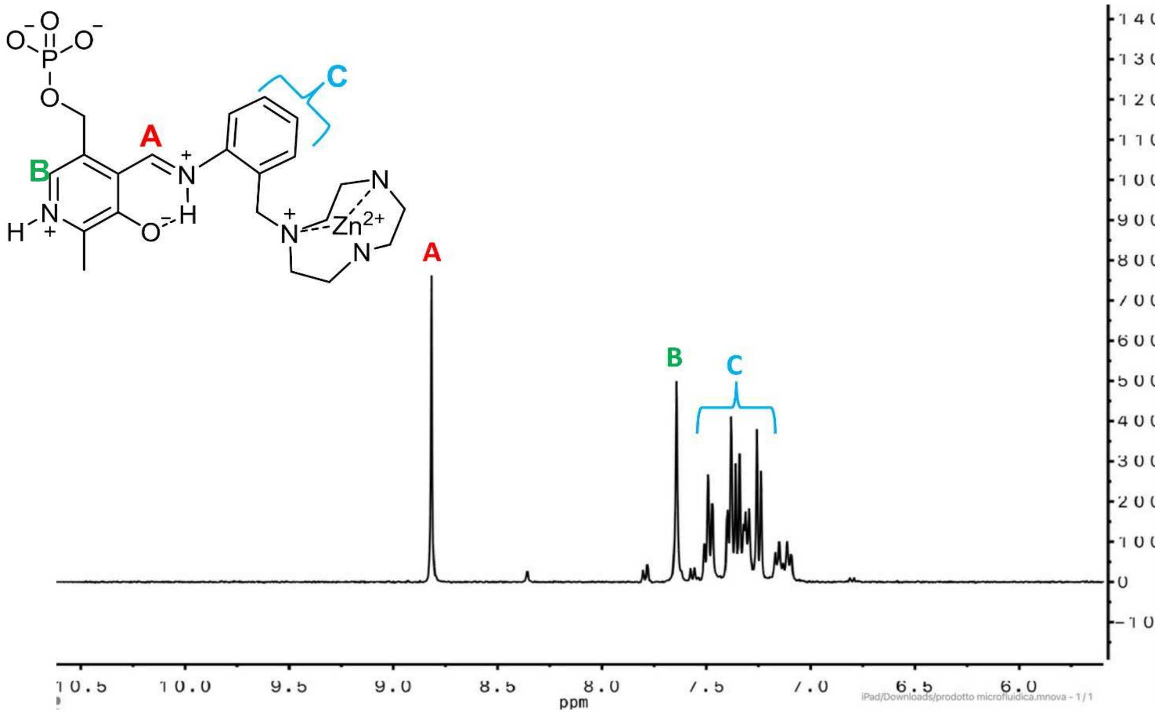

Figure 2.5.9: proton NMR spectra of the reaction solution, recorded at 400 MHz and in H_2O:D_2O solvent in 9:1 ratios. Highlighted in the spectrum are the peak of the imine proton at 8.8 ppm, singlet (A), the peak for the pyridine proton at 7.6 ppm, singlet (B) and the aromatic protons from 7.5 to 7.2 ppm (C).

2.5.2 Considerations on the reaction mechanism

As already mentioned at the beginning of Chapter 2.4, although the mechanism of Schiff base formation is well known and studied in basic organic chemistry courses, the reason why PLP and Aniline-TACN(Zn) undergo this quantitative reaction so fast is still under debate. In particular, the synergic role played by the phosphate group in PLP, and the TACN(Zn) in the Aniline residue was already proved to be the key factor. Some hypotheses can be made on the mechanism by which these two reagents undergo the reaction, and on the structure of the product, based on deep inspection of the experimental SERS and H-NMR spectra, DFT simulations and information available in specialized literature.

First of all, pKa values calculated for PLP and imines formed by PLP with a variety of amino acids can help to predict the protonation state of the molecules under investigation. For PLP, the oxygens on the phosphate group have a pKa of 5.90, the phenolic group of 3.58 and the pyridine nitrogen of 8.33.[50] This means that at pH 7, which is the pH maintained by us during the reaction with the HEPES buffer, only the nitrogen is protonated. For a Schiff base formed by PLP and glycine, the pKa values for the product were: 5.46 (phosphate), 2.40 (phenol), 6.36 (pyridine), 11.35 (imine nitrogen), indicating that at a neutral pH the two nitrogens are protonated.[50] Protonation of the imine nitrogen has a stabilizing effect on the imine itself, because it is involved in a hydrogen bond with the phenolic oxygen.[50] Indeed, it is reported that the same stabilization is also provided by coordinating a metallic cation.[8]

Another important aspect for the high velocity and yield of the reaction is the phosphate group. By preliminary data provided by Doc. Gabrielli's group, the same reaction done with pyridoxal, which has the same structure as PLP but with an OH group instead of the phosphate, reaches yields of 70% only after 20 days. A possible explanation for this is that the OH and the carbonyl group in pyridoxal can form a cyclic hemiacetal, which reduces the concentration of free aldehyde for the reaction with the amine.[51] The phosphate group in PLP, on the other hand, does not undergo the same cyclization, with the effect of making the reaction more quantitative.[51] However another explanation is possible, indeed reasonably complementary, which involves both the phosphate group and the zinc cation. Zn(II) generally has coordination numbers from 4 to 6,[52] so different coordination structures are possible. Zn^{2+} is also known to undergo rapid ligand exchange, seamlessly changing its coordination number.[53] In particular, Zn(II)-polyamine complexes have been extensively studied to model Zn-based enzymes, and have been shown to have reversible coordination with phosphate anions, even acting as a bridge between TACN and phosphate ligands like in the complexes synthesised by Fry *et al* [54]. This suggests that an extended coordination of the Zn^{2+} between TACN and the phosphate group could be responsible for keeping the reagents together during the formation of the imine, in addition to stabilizing the product. This hypothesis finds support by the optimized geometry obtained by the DFT simulations already used in Table 3, that foresees the Zn cation bridging the TACN and phosphate group, almost the same arrangement previously reported by Fry at al[54].

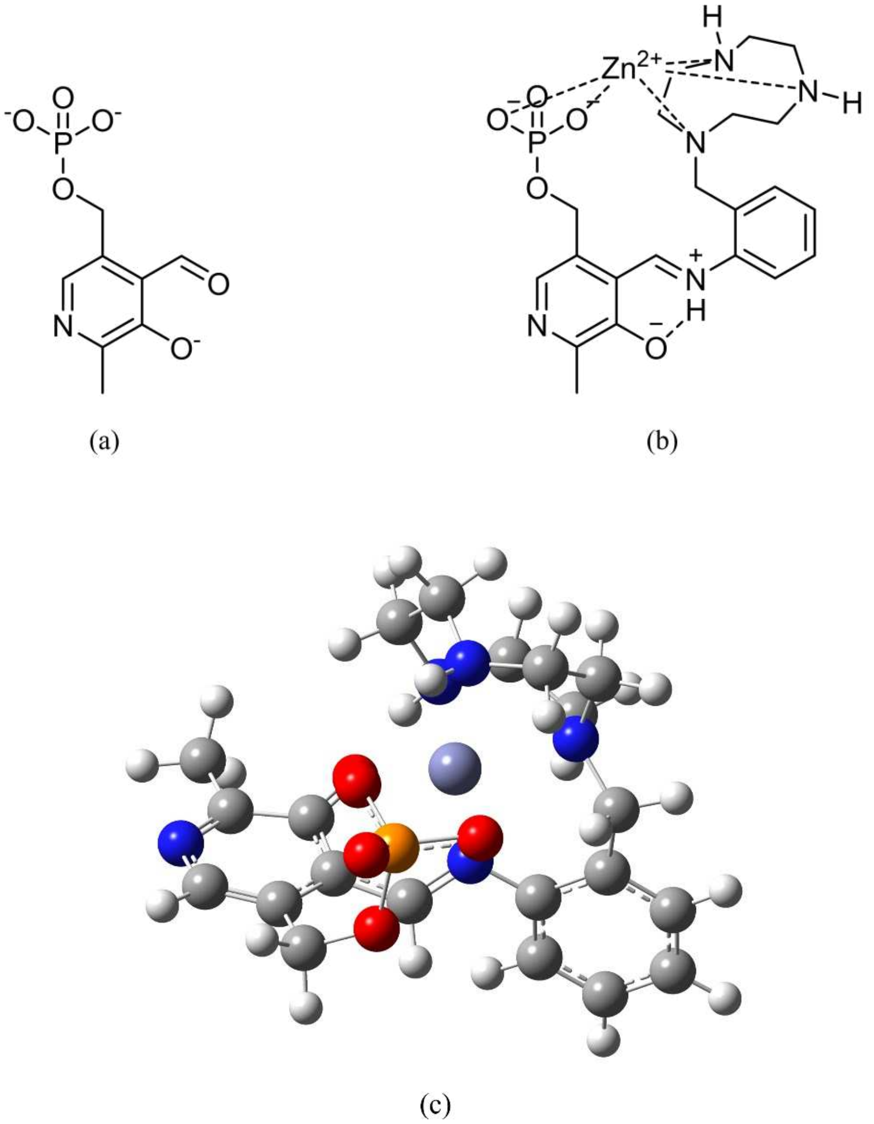

Figure 2.5.10: ionic forms of PLP (a) and the Schiff base product (b) in aqueous solvent at pH 7; (c) molecular structure of the product, as optimized by DFT simulations. The Zn^{2+} cation is clearly visible between the phosphate group and the TACN group.

3 Materials and Methods

3.1. Instruments

Dimatix Materials Printer

The inkjet printer used in this project is the Dimatix Materials Printer DMP-2800 (Fujifilm), equipped with cartridges capable of ejecting 10 pL droplets through each of the 16 piezoelectric nozzles. The main components of the printer are:

- the cartridge holder, which hosts the ink cartridge
- the platen, which keeps the substrate steady during the printing process thanks to a light vacuum
- the fiducial camera, which shows the substrate on the platen
- the drop watcher, another camera which shows the printing nozzles.

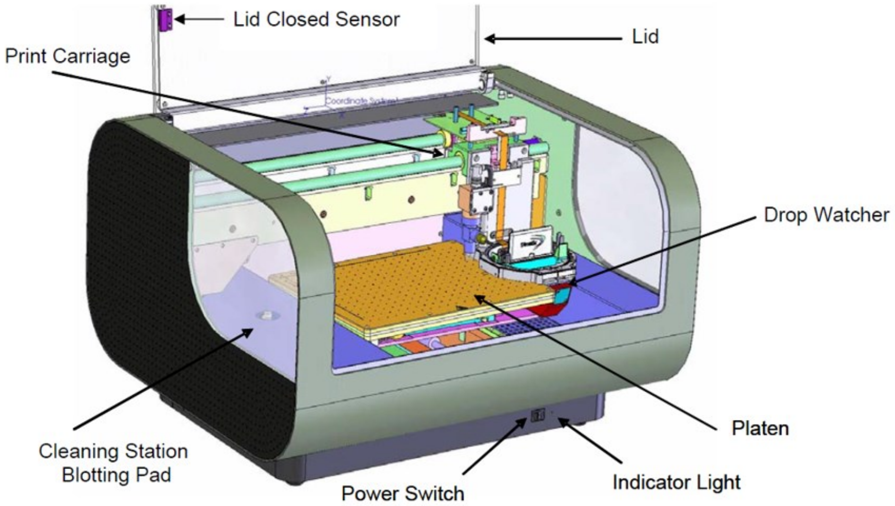

Figure 3.1: schematic representation of Dimatix DMP-2800 from the user manual.

The printer is controlled through the *Dimatix Drop Manager* software, where the user can upload and modify patterns, optimize the waveform and choose cartridge settings and printing parameters, like the cartridge temperature, the firing voltage and printing resolution.

Raman spectrometer

Raman measurements were taken with the Renishaw inVia μRaman, represented schematically in Figure 3.1.2. The instrument is equipped with three laser sources: a HeNe laser emitting at 633 nm, an Argon laser emitting at 488 and 514 nm and finally a diode laser emitting at 785 nm. The light of the chosen wavelength is expanded in a series of parallel rays by a beam expander and arrives on the sample guided by some mirrors and focused with an optical microscope. The scattered light is again collected by the same microscope and filtered by an edge filter to remove the Rayleigh scattering, then it passes through a diffraction grating that splits into component wavelengths. The spectrum is finally detected by a CCD camera, where each pixel generates an electric current when hit by a photon.

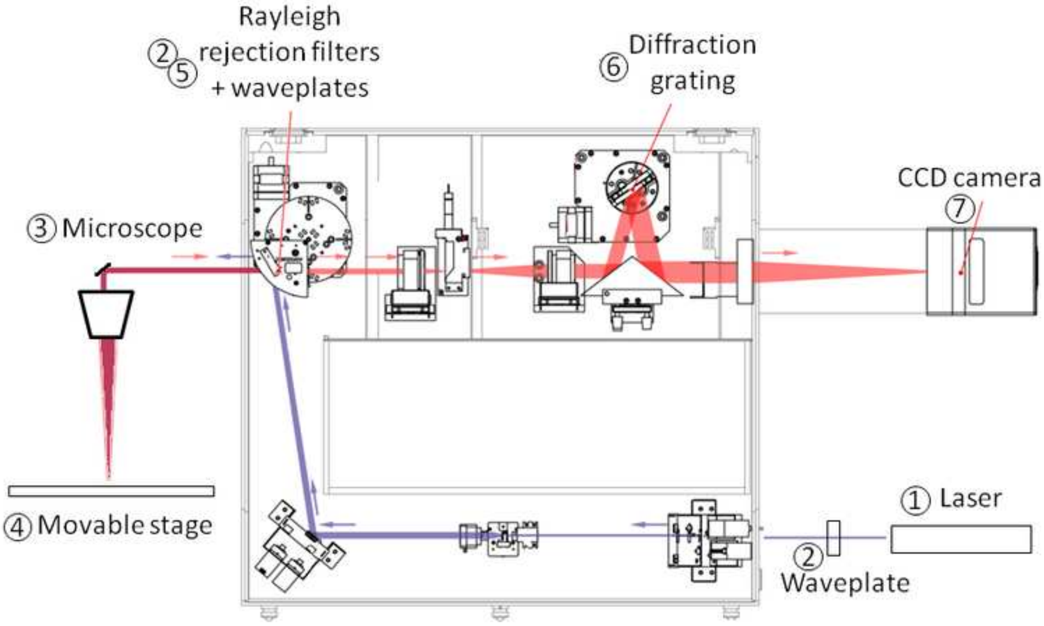

Figure 3.2: schematic representation of a Raman spectroscope, adapted from Renishaw documentation.

The spatial resolution of a micro-Raman measure depends on the wavelength of the laser and on the numerical aperture of the microscope objective, as expressed by the formula $d = 1.22\frac{\lambda}{NA}$.

UV-visible-NIR spectrometer

Absorbance measurements were taken with Agilent Cary 5000 UV-vis-NIR spectrometer.

Syringe pumps

The programmable syringe pumps used in the microfluidic experiments were model NE-300 from KF Technology. This model is capable of pumping continuously at a programmable infusion rate, thanks to a step motor led by a microcontroller. Figure 3.1.3 shows the experimental set up during the experiment with Nile Blue and Crystal Violet.

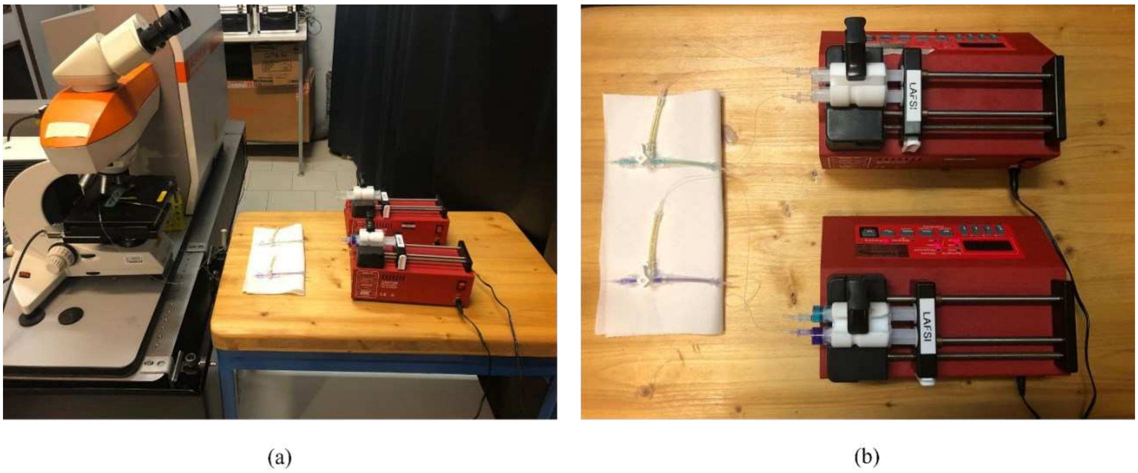

(a) (b)

Figure 3.3: (a) experimental setup with the two syringe pumps, the valves and the microfluidic chip under the Raman microscope; (b) close-up of the two syringe pumps loaded with water and the two dyes.

3.2 Materials

- NaCl, VWR Chemicals
- Polyvinyl alcohol (PVA), 22000 Da, Fluka
- Isopropanol (IPA), Sigma-Aldrich
- Hamilton cleaning solution 18310
- Acetone, Sigma-Aldrich
- Polydimethylsiloxane (PDMS), Sylgard 184, Dow Corning

- PTFE tubing, Sigma-Aldrich
- Silicon bicomponent glue, Picodent
- Nile Blue A perchlorate, Aldrich
- Crystal Violet, Aldrich
- Methylen Blue, supplied by the guesting group
- Fluoresceine, supplied by the guesting group
- Pyridoxal 5'-phosphate (PLP), supplied by Doc. Luca Gabrielli's group
- Aniline functionalized with 1,4,7-triazacyclononane (TACN) and Zn^{2+}, supplied by Doc. Luca Gabrielli's group

3.3 SERS substrates production

3.3.1 Ink production

Laser Ablation

Gold nanoparticles were produced by laser ablation (LASiS) of a gold target in acqueous solvent (NaCl 10 µM in bidistilled water). The ablation was carried out in continuous mode, by irradiating the target placed in a glass flask connected to the solvent reservoir and to a peristaltic pump. The apparatus allowed for the continuous increase of nanoparticles concentration in the solvent, until the UV-vis absorption spectrum of the solution reached 0.7, corresponding to a nanoparticle concentration of 1.88 nM, calculated according to the method presented in reference 42. The Nd:YAG laser (Quantel QSmart 850) operated ad 1064 nm with 9 ns pulses with a 20 Hz frequency, the fluence was adjusted as 1 J/cm^2.

Ink formulation

A 10 mg/mL solution of PVA was obtained by dissolving 50 mg of PVA in 5 mL of bidistilled water at 69°C. The PVA solution was then added to the colloidal suspension obtained by LASiS in 24 Eppendorf vials (1.5 mL), with a 1:9 proportion (100 µL PVA and 900 µL AuNPs). The vials were then centrifuged at 2500 rcf for 30 minutes, the supernatant was removed and all the precipitate collected in a single vial, which then underwent a final centrifugation cycle. This process was repeated 4 times with new batches of AuNP-PVA solution and the precipitate of the last concentration steps was collected, obtaining around 2 mL of ink with a final concentration of $2.3 \cdot 10^{-8}$ M (in nanoparticles).

3.3.2 Inkjet printing process

The first step in the printing process is designing the pattern. The free software *Inkscape* was used to generate a *.png* file at a resolution of 1693 dpi, which was subsequently converted in monochromatic bitmap and loaded on the printer software. The substrates (1 mm glass slides by Thermo Fisher Scientific and 1.5 mm aluminium slides) were cleaned firstly with dish soap, then with subsequent sonication in acetone and IPA for 15 minutes each. Before being loaded with the ink, the cartridge was cleaned to free the nozzles from residual ink and PVA occlusions: firstly it was sonicated in Hamilton cleaning solution and then in IPA, then it was immersed in boiling water for one hour. The cartridge's reservoir was then filled with IPA and used to print a reference pattern to further clean up the nozzles and to check that they were firing (thanks to the drop watcher camera). In the meantime, the ink was degassed by sonication for about 20 minutes and loaded into a syringe. After printing with IPA, the nozzles were carefully dried with a flow of N_2 and the cartridge's reservoir was loaded with the ink. The drop watcher camera was used to check the nozzles and to select the one with the most uniform firing behaviour. After choosing the firing voltage, the waveform and the print settings, like the number of layers, printing was initiated. Figure 3.3.1 shows a photo of an obstructed nozzle and the waveform used for printing. For printing the SERS substrate later used as the microfluidic bottom surface, the voltage was set between 20 and 30 V and the prints were done with 15 µm drop spacing, in two layers when printed on glass (for the PDMS chip) and in 3 layers when printed on aluminium (for the brass chip).

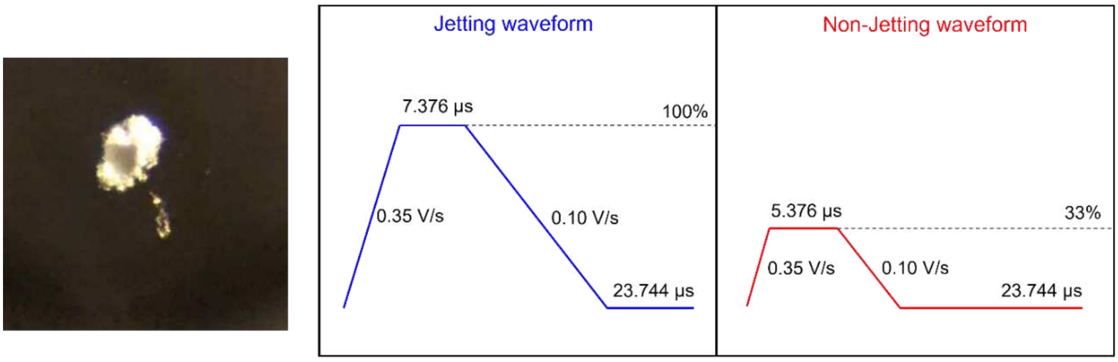

(a) (b)

Figure 3.3.1: (a) photograph of a nuzzle obstructed with PVA, taken with a 40x objective; (b) the waveform optimized for printing water-based inks.

After printing, the substrates were placed in an oven at 500°C for three hours under air flux to remove the PVA.

3.4 Dyes and reaction study

Solutions

For the mixing study done on Nile blue, Crystal violet and Methylene blue, 10 mL solutions with 20 µM concentration of each dye were prepared. Initially, concentrated solutions (4 mM) were made by dissolving 0.0033 g of Nile blue (417.84 g/mol), 0.0033 g of Crystal violet (407.98 g/mol) and 0.0025 g of Methylene blue (319.85 g/mol) in 2 mL of bidistilled water. Then, to obtain the three final solutions, 50 µL of each were with 9.95 mL of bidistilled water.

For the reaction study, reagents supplied by Luca Gabrielli's group were diluted in milliQ water and buffered with HEPES, to obtain 8 mL of reactants solutions 1 mM in PLP and Aniline-TACN(Zn) and 20 mM in HEPES. The latter were the starting solutions already used by the group of Dr. Gabrielli for the same reaction, so that the kinetic and yield were already known on these conditions. For the preliminary study done on drop-casted AuNP, the imine product synthesized by

Luca Gabrielli's group was also analysed, diluted to 1mM from the original solution. The exact dilutions are reported in Table 1.

Table 1: dilutions used to prepare the solutions for the microfluidic experiment. The dilutions indicated on the Product on the other hand refer to the 400 µL of solutions used for the reference spectrum.

Substance	Original Concentration	Quantity	Final Concentration
PLP	10 mM	0.8 mL	1 mM
Aniline-TACN(Zn)	4 mM	2 mL	1mM
Product	2 mM	100 µL	1 mM
HEPES	100 mM	1.6 mL	20 mM

DFT calculations

The DFT calculations were carried out with Gaussian, optimizing the molecular structures with B3LYP functional and 6-311+G(d,p) basis set for the molecules in free space. The optimized structures were then subjected to Raman spectra calculations.

3.5 Chip construction

3.5.1 PDMS chip

The PDMS chip was constructed by replica molding with polydimethylsiloxane of a master prepared by photolithography. Initially, the non-polymerized PDMS was mixed with the curing agent, degassed and poured in the mold, then placed in an oven at 70 °C for 40 minutes. After curing, the PDMS was peeled off and a puncher was used to create the holes for the inlets and the outlet. An oxygen plasma was then used to bond the chip to the printed glass slide. PTFE tubes (0.3mm inner diameter) were attached to the holes with an epoxy glue. The three inlet channels had a nominal height off 100 µm and 700 µm width, with the main channel 2.1 mm wide and 3 cm long.

Figure 3.5.1: channel design for the PDMS chip.

3.5.2 Brass chip

The brass chip was made by Doc. Ferraro's group via micro-milling of a 0.5 mm thick brass sheet. The outside perimeter of the channel was also hollowed out so that a 0.2 mm high step surrounded the channel, to avoid the silicon glue coming in. The aluminium slides were cut from a 1.5 mm aluminium sheet, while the glass cover slides were sandwiched between a 3D printed mask and sandblasted to obtain the holes for inlets and outlets. The silicon glue was mixed with its catalyser and then manually spread on the two sides of the brass chip to assemble them. Two glass slides (0.15 mm high and 60 cm long) were necessary to cover the whole chip, so a thin line of silicon glue was used to close the gap between them from the top.

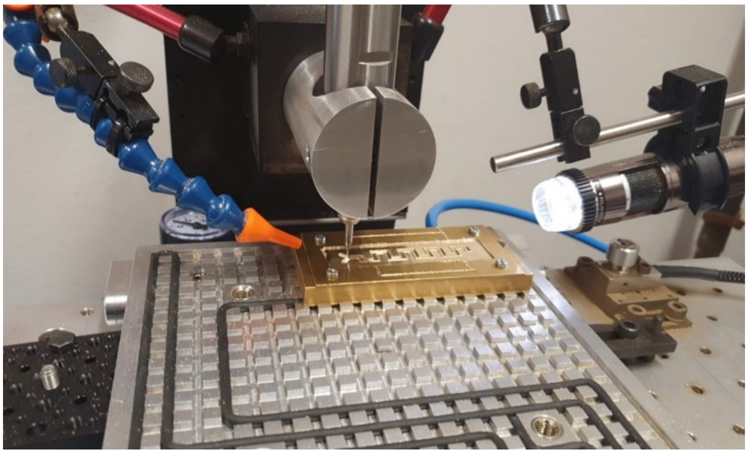

Figure 3.5.2: micro-milling machine hollowing out the chip from the brass sheet.

The dimensions of the chip were calculated based on the reaction time and the flow velocity. A 115 mm channel would have allowed for a maximum flow velocity of 1.9 µL/min, so a 1.5 µL/min flow was prudently chosen. Table 2 reports calculations for the chip length.

Table 2: Calculations for the chip length for a 1.9 µL/min flow.

Flow velocity	1.9 µL/min	1.5 µL/min
Reaction Time	60 min	60 min
V	114 mm^3	90 mm^3
z	500 µm	500 µm
y	2000 µm	2000 µm
Channel Lenght for the reaction to occur	114 mm	90 mm

4 Conclusions

This thesis work explores the development of an *in situ*, label free sensor integrated within a microfluidic chip, capable of investigating the reaction dynamics toward an imine formation. In order to address this task, the bottom wall of the chip was inkjet-printed with an optimized Au nanoparticles ink, obtaining the right attributes to be used as Surface Enhanced Raman Spectroscopy substrates.

Initially, Laser Ablation Synthesis in Solution (LASiS) was used as a top-down method to produce Au nanoparticles as a stable colloid, without the need of a capping agent. The gold colloid was then transformed in printable ink with the addition of PVA and through a series of centrifugation steps. Finally, the ink was used to print the bottom side of the chip (either glass or aluminium slides) through a drop-on-demand inkjet printer.

Two chip constructions were tested, together with reference mixtures of dyes used because of their clear SERS response. A PDMS and glass chip was used to optimize the experimental setup which allowed for the synchronous entry of the mixture components in the main channel, always under a laminar flow regime. The setup was validated by the injection of three non-interacting dyes. Their relative routes within the chip were revealed by *in situ* SERS measures.

These findings were used in the study of the Schiff base formation from PLP and Aniline-TACN(Zn). Firstly, Raman spectra of the reactants and product were collected on drop-casted gold nanoparticles. DFT calculations were used to attribute the main peaks ascribed to each species.

A new chip concept was then designed for the reaction to occur, with a longer serpentine channel that ensured mixing of the reactants, and for the 785 nm laser wavelength as the best choice to obtain clear spectra. The reaction system proved to be challenging to investigate with respect to the dyes, but multivariate principal component analysis was capable to reveal the spatial patterns of the reactants and product inside the chip. Further efforts to make the chip more sensible to the reactive system could be made by optimizing the SERS substrate to improve the adsorption of the molecules, while a quartz slide would solve the issue of the glass photoluminescence and allow for a more reproducible and stable chip construction. Finally, the interplay between TACN(Zn) and phosphate group, belonging to the two reagents, was hypothesised thanks to experimental and DFT Raman spectra, with the Zn^{2+} cation bridging between the phosphate group of PLP and the TACN group, keeping the two reactants together and thus favouring the reaction yield as well as speeding up the overall kinetics. All of these highlight the great potential of Raman, implemented as the SERS technique, in studying chemical reaction *in situ* within microfluidic devices.

Bibliography

1. Whitesides, G. M. The origins and the future of microfluidics. *Nature* vol. 442 368–373 (2006).

2. Nguyen, N.-T. & Wereley, S. T. *Fundamentals and Applications of Microfluidics Second Edition*. (2006).

3. Schetz, J. A. & Fuhs, A. E. *Fundamentals of fluid mechanics*. (John Wiley & Sons, 1999).

4. Folch, A. FolchLab Picture Gallery. https://albertfolch.wixsite.com/folchlabhome/picasa-gallery.

5. Suh, Y. K. & Kang, S. A review on mixing in microfluidics. *Micromachines* vol. 1 82–111 (2010).

6. Beebe, D. J., Mensing, G. A. & Walker, G. M. Physics and applications of microfluidics in biology. *Annual Review of Biomedical Engineering* vol. 4 261–286 (2002).

7. DeMello, A. J. Control and detection of chemical reactions in microfluidic systems. *Nature* 442, 394–402 (2006).

8. Sackmann, E. K., Fulton, A. L. & Beebe, D. J. The present and future role of microfluidics in biomedical research. *Nature* vol. 507 181–189 (2014).

9. Liu, Y. & Jiang, X. Why microfluidics? Merits and trends in chemical synthesis. *Lab Chip* 17, 3960–3978 (2017).

10. Brivio, M., Verboom, W. & Reinhoudt, D. N. Miniaturized continuous flow reaction vessels: Influence on chemical reactions. *Lab on a Chip* vol. 6 329–344 (2006).

11. Plutschack, M. B., Pieber, B., Gilmore, K. & Seeberger, P. H. The Hitchhiker's Guide to Flow Chemistry. *Chemical Reviews* vol. 117 11796–11893 (2017).

12. Huang, C.-W. *et al.* Efficient SNP Discovery by Combining Microarray and Lab-on-a-Chip Data for Animal Breeding and Selection. *Microarrays* 4, 570–595 (2015).

13. Leung, S. A., Winkle, R. F., Wootton, R. C. R. & DeMello, A. J. A method for rapid reaction optimisation in continuous-flow microfluidic reactors using online Raman spectroscopic detection. *Analyst* 130, 46–51 (2005).

14. Li, J. *et al.* In situ sensors for flow reactors-A review. *Reaction Chemistry and Engineering* vol. 6 1497–1507 (2021).

15. Hartman, R. L., McMullen, J. P. & Jensen, K. F. Deciding whether to go with the flow: Evaluating the merits of flow reactors for synthesis. *Angewandte Chemie - International Edition* vol. 50 7502–7519 (2011).

16. Schüth, F., Bussian, P., Ågren, P., Schunk, S. & Lindén, M. *Techniques for analyzing the early stages of crystallization reactions. Solid State Sciences* vol. 3 (2001).

17. Yan, Z., Tian, J., Du, C., Deng, J. & Luo, G. *Reaction Kinetics Determination Based on Microfluidic Technology.*

18. Zhou, P., He, H., Ma, H., Wang, S. & Hu, S. A Review of Optical Imaging Technologies for Microfluidics. *Micromachines* vol. 13 (2022).

19. Sarrazin, F., Salmon, J. B., Talaga, D. & Servant, L. Chemical reaction imaging within microfluidic devices using confocal raman spectroscopy: The case of water and deuterium oxide as a model system. *Anal Chem* 80, 1689–1695 (2008).

20. Xie, W., Grzeschik, R. & Schlücker, S. Metal Nanoparticle-Catalyzed Reduction Using Borohydride in Aqueous Media: A Kinetic Analysis of the Surface Reaction by Microfluidic SERS. *Angewandte Chemie* 128, 13933–13937 (2016).

21. Smith, Ewen. & Dent, Geoffrey. *Modern Raman spectroscopy: a practical approach.* (J. Wiley, 2005).

22. Kumar, D., Manik, S., Arnulf, P. & Editors, M. *Progress in Optical Science and Photonics Modern Techniques of Spectroscopy Basics, Instrumentation, and Applications.*

23. Butler, H. J. *et al.* Using Raman spectroscopy to characterize biological materials. *Nat Protoc* 11, 664–687 (2016).

24. le Ru, E. C. & Etchegoin, P. G. *Principles of surface-enhanced Raman spectroscopy and related plasmonic effects.* (Elsevier, 2009).

25. Long, D. A. *The Raman Effect.* (2002).

26. Fleischmann, M., Hendra, P. J. & McQuillan, A. J. Raman spectra of pyridine adsorbed at a silver electrode. *Chem Phys Lett* 26, 163–166 (1974).

27. Willets, K. A. & van Duyne, R. P. Localized Surface Plasmon Resonance Spectroscopy and Sensing. *Annu Rev Phys Chem* 58, 267–297 (2007).

28. Kneipp, K. Surface-enhanced Raman Scattering. *Phys Today* 60, 40–46 (2007).

29. Maher, R. C. SERS Hot Spots. in *Raman Spectroscopy for Nanomaterials Characterization* 215–260 (Springer Berlin Heidelberg, 2012).

30. Ricci *et al.* Inkjet-printed Au nanoparticles as SERS substrates and microelectrodes, submitted. (2022).

31. Langer, J. *et al.* Present and Future of Surface-Enhanced Raman Scattering. *ACS Nano* 14, 28–117 (2020).

32. *Colloidal Gold.* (Elsevier, 1991).

33. Huang, X. & El-Sayed, M. A. Gold nanoparticles: Optical properties and implementations in cancer diagnosis and photothermal therapy. *J Adv Res* 1, 13–28 (2010).

34. Eastman, J. *Colloid Science: Principles, Methods and Applications.* (2005).

35. Russo, R. E., Mao, X. L., Yoo, J. & Gonzalez, J. J. Laser ablation. in *Laser-Induced Breakdown Spectroscopy* 41–70 (Elsevier, 2007).

36. Amendola, V. & Meneghetti, M. Laser ablation synthesis in solution and size manipulation of noble metal nanoparticles. *Physical Chemistry Chemical Physics* 11, 3805–3821 (2009).

37. Xu, X. *et al.* Fabrication of Gold Nanoparticles by Laser Ablation in Liquid and Their Application for Simultaneous Electrochemical Detection of Cd^{2+}, Pb^{2+}, Cu^{2+}, Hg^{2+}. *ACS Appl Mater Interfaces* 6, 65–71 (2014).

38. Beedasy, V. & Smith, P. J. Printed electronics as prepared by inkjet printing. *Materials* vol. 13 (2020).

39. *Reactive Inkjet Printing: A Chemical Synthesis Tool.* (Royal Society of Chemistry, 2017).

40. Abbas, A. Inkjet Printing of Ag Nanoparticles using Dimatix Inkjet Printer, No 1.

41. Singh, M., Haverinen, H. M., Dhagat, P. & Jabbour, G. E. Inkjet Printing-Process and Its Applications. *Advanced Materials* 22, 673–685 (2010).

42. Litti, L. & Meneghetti, M. Predictions on the SERS enhancement factor of gold nanosphere aggregate samples. *Physical Chemistry Chemical Physics* 21, 15515–15522 (2019).

43. Boin, D. Produzione di inchiostri a base di nanoparticelle plasmoniche e relativa applicazione in stampanti a getto d'inchiostro. (Università degli Studi di Padova, 2022).

44. Nayak, L., Mohanty, S., Nayak, S. K. & Ramadoss, A. A review on inkjet printing of nanoparticle inks for flexible electronics. *J Mater Chem C Mater* 7, 8771–8795 (2019).

45. Thomas, P. S., Guerbois, J.-P., Russell, G. F. & Briscoe, B. J. FTIR Study of the Thermal Degradation of Poly(vinyl Alcohol). *J Therm Anal Calorim* 64, 501–508 (2001).

46. Angel Vazquez, M., E, F. M., Donoso, J. & Garcia Blanco, F. *Kinetic Study of the Schiff-base Formation between Glycine and Pyridoxal 5'-Phosphate (PLP), Pyridoxal (PL), and 5'-Deoxypyridoxal (DPL).* (1989).

47. Dajnowicz, S. *et al.* Direct visualization of critical hydrogen atoms in a pyridoxal 5′-phosphate enzyme. *Nat Commun* 8, (2017).

48. Matsuo, Y. Formation of Schiff Bases of Pyridoxal Phosphate. Reaction with Metal Ions.

49. Bruice, P. Y. *Organic Chemistry.* (Pearson College, 2016).

50. Angel Vazquez, M., E, F. M., Donoso, J. & Garcia Blanco, F. *Kinetic Study of the Schiff-base Formation between Glycine and Pyridoxal 5'-Phosphate (PLP), Pyridoxal (PL), and 5'-Deoxypyridoxal (DPL).* (1989).

51. Snell, E. E. & di Mari, S. J. Schiff Base Intermediates in Enzyme Catalysis. *Enzymes (Essen)* 2, 335–370 (1970).

52. Housecroft, C. E. & Sharpe, A. G. *Inorganic Chemistry.* (Pearson, 2018).

53. Kumar, N., Roopa, Bhalla, V. & Kumar, M. Beyond zinc coordination: Bioimaging applications of Zn(II)-complexes. *Coordination Chemistry Reviews* vol. 427 (2021).

54. Fry, F. H., Jensen, P., Kepert, C. M. & Spiccia, L. Macrocyclic copper(II) and zinc(II) complexes incorporating phosphate esters. *Inorg Chem* 42, 5637–5644 (2003).

Ringraziamenti

A conclusione di questo percorso, ci tengo a ringraziare le persone il cui aiuto è stato essenziale per raggiungere questo risultato.

Prima di tutto il Dott. Lucio Litti, che mi ha guidato con disponibilità e pazienza, aiutandomi non solo con i problemi del laboratorio ma offrendo anche preziosi consigli di vita. Ringrazio anche il Prof. Moreno Meneghetti per avermi accolto nel gruppo e per essere sempre stato disponibile a rispondere alle mie domande o ad offrire un consiglio, e Anna, Giulia e Francesco del gruppo NOL per il divertimento che ha alleggerito anche i momenti più difficili.

Ringrazio in particolare il Dott. Davide Ferraro e i ragazzi del gruppo LaFSI per avermi ospitato nel loro laboratorio e per avermi seguito con grande disponibilità e pazienza nella creazione dei chip microfluidici. Grazie al Dott. Luca Gabrielli e a Tommaso per l'aiuto con la reazione, e per aver risposto anche oltre le aspettative a tutte le mie domande.

Ringrazio il mio controrelatore, il Dott. Daniel Forrer, per essere stato sempre gentile e accurato nelle sue osservazioni. Un ringraziamento va anche al Prof. Flavio Maran per avermi dato la possibilità di usare la stampante inkjet.

Ringrazio di cuore i miei genitori, Pietro e Serena, per essere sempre stati una roccia nel momento del bisogno. Infine, ringrazio Leonardo per essere stato al mio fianco e per avermi sempre trascinata fuori di casa, salvandomi dal venire sepolta dai libri.